ION IMPLANTATION DAMAGE IN GaAs AT LOW TEMPERATURES

ION IMPLANTATION DAMAGE IN GaAs AT LOW TEMPERATURES

by

AHMAD M.M. IBRAHIM, B.Sc. (EE)

A Thesis

Submitted to the School of Graduate Studies

in Partial Fulfilment of the Requirements

for the Degree

Master of Engineering

McMaster University

May 1982

MASTER OF ENGINEERING (1982) McMASTER UNIVERSITY
Department of Engineering Physics Hamilton, Ontario

TITLE: Ion Implantation Damage in GaAs at Low Temperatures

AUTHOR: Ahmad M.M. Ibrahim, B.Sc. (Ain Shams)

SUPERVISOR: Professor D.A. Thompson

NUMBER OF PAGES: viii, 100

ABSTRACT

This thesis reports on the investigation of damage production in GaAs at low temperature using the channeling-backscattering technique.

The study has been divided into two parts; first, the investigation of damage produced by 2 MeV helium ions in unimplanted and previously implanted samples with varied doses of 40 keV nitrogen and bismuth. The helium beam damage has been found to depend on the initial state of damage of the samples. In the second part the damage production due to 40 keV N^+, As^+, Sb^+ and Bi^+ ion implantation has been investigated. A comparison with damage production due to the corresponding 80 keV diatomic implants has also been carried out. No enhancement in the damage production was noticed due to the molecular implants.

ACKNOWLEDGEMENTS

I wish to express my sincere gratitude to my Supervisor, Professor D.A. Thompson, for his continuous support and guidance throughout the course of this work.

I wish also to thank Professor J.A. Davies, whose comments have been extremely valuable.

I would like to express my gratefulness to Professor G. Carter for his suggestions that promoted this work.

Thanks are also due to D. Stevanovic for the technical help and the useful discussions. I also acknowledge the cooperation of N. Parikh, R. Macaully-Newcombe and U. Akano.

TABLE OF CONTENTS

LIST OF FIGURES

CHAPTER I

INTRODUCTION

Ion implantation is now a standard technique for doping semiconductors[1].

This technique has several advantages; the doping level can be more accurately controlled than the thermal diffusion technique, especially when very low doping is required. Also, the penetrating depth of the dopants can be controlled accurately and depth profiles can be tailored simply by varying the energy and dose of the ions.

An important advantage is that, in principle, any element can be implanted. Also, ion implantation may represent an ideal technique for doping compound semiconductors where the problem of surface decomposition needs to be faced. A disadvantage of ion implantation occurs as a result of the dissipation of energy to the crystal lattice as the ion slows down. This process produces damage[2]. Annealing treatments are usually necessary to remove the lattice disorder and to attain the required electrical characteristics[3,4].

It is ironic that the first reported[5] use of ion implanation to improve the characteristics of a semiconductor device was based on introducing surface damage rather than chemical doping.

Since the important role that the damage plays was realized, the investigations of radiation damage have been carried out as a function of all combinations of implantation conditions; i.e. ion species, energy, implantation temperature, does, beam current and the properties of the semiconductor itself. Si and Ge have been extensively studied and their behavior is basically understood. Currently, GaAs is receiving much attention[6].

In order to study the damage as produced, measurements have to be carried out at temperatures low enough to inhibit or at least minimize the annealing of damage. At higher temperatures, implantation dose-rate effects also appear[7,8].

A widely used technique for analysing the damage is Rutherford backscattering combined with the channeling technique[9]. However, it has been noted[10] that this technique may contribute significantly to the damage production especially for very low implant doses ($\lesssim 10^{13}$ cm^{-2}).

This thesis reports on the investigations of damage produced in GaAs at low temperatures by the analysing $^4He^+$ beam probe under different levels of prior ion implantation damage. It also reports on the damage produced by heavy ions in GaAs at low temperatures.

CHAPTER II

GaAs REVIEW

2-1 Introduction

GaAs is an attractive material from the point of view of device fabrication. Since it has high mobility (four to six times than that of Si), it is applicable for high speed devices[11]. Also, GaAs can operate in a higher temperature environment and can tolerate the higher temperatures produced during high speed operation without excessive leakage currents[12]. Due to the particular nature of the GaAs band structure, its bulk properties can be used to produce microwave oscillations under certain biasing conditions[13]. It also has applications in optoelectronic devices which include; infrared sources[14], lasers[15], detectors and solar cells[16].

Unfortunately, technological difficulties have slowed the development of GaAs devices. The difficulty of doping GaAs may be solved by ion implantation. Another difficulty has been the production of high quality GaAs crystals, this problem is under active investigation and the growth of high purity semi-insulating GaAs crystals suitable for ion implantation has been recently reported[17,18].

In the following sections some of the most important features of GaAs will be discussed.

2-2 Crystal structure

The crystal structure of GaAs is of the zinc-blende type[19]. Zincblende structure is basically a diamond structure, where each atom lies in the center of a tetrahedron formed by four nearest neighbours, however, nearest neighbour points are occupied by different elements, namely, Ga and As.

Fig. (2-1) shows schematically the side and top view of GaAs structure (100). (110) and (111) surfaces[20]. It is apparent that identical hexagonal rings are stacked upon each other in the <100> direction. Every atom in the (100) surface is bound by two of its sp^3-bonds to atoms of the layer lying just below. The other two bonds are dangling. The structure is independent of whether the topmost layer is formed by Ga or As atoms. The (110)-surface contains an equal number of Ga and As atoms. Every atom is connected by one bond with the next lower-lying layer. Two bonds extend in the surface plane to the two next-nearest neighbours, and the fourth bond is dangling. For (111)-surfaces the topmost atomic plane contains only Ga atoms or only As atoms. Either of these can be connected by three bonds with three atoms of the next lower-lying layer, with one dangling bond remaining.

Referring to the side view given in Fig. (2-1); the distances between the outermost layers are[20];

$\frac{1}{4}$ a for (100) face

$1/[2\sqrt{2})]$a for (110) face

and $(\sqrt{3}/4)$a for the (111) face

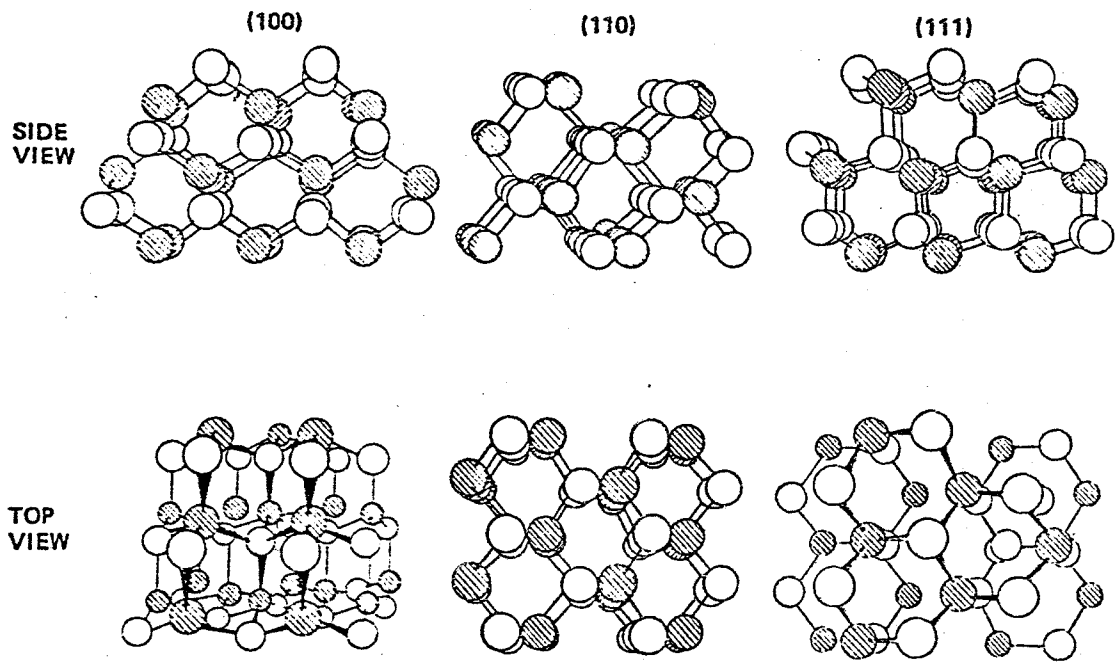

Fig. (2-1) The side and top views of GaAs crystal. (Ref. 20)

where a is the lattice parameter; its value at room temperature is 5.675 Å.

2-3 Binding

The bonding of GaAs is a mixture of ionic and covalent bonding[19]. The wave function of the bond is built up with the wave functions of the two extreme cases of pure covalent binding and ionic binding;

$$\psi = (1-\lambda)^{1/2} \psi_{cov} + \lambda^{1/2} \psi_{ion} \qquad (2\text{-}1)$$

λ being a measure of the ionicity of the bond, its value for GaAs is 1/4 and this corresponds to neutral binding[19].

The "heat of atomization" or the "cohesive energy" can be used as a measure of the binding strength. For GaAs, cohesive energy is 76 Kcal/mole of compound[21], while it is 89 Kcal/mole for Ge[22]. Therefore, GaAs is less strongly bound than Ge.

2-4 Threshold displacement energy, E_d

The threshold displacement energy is one of the important parameters in the study of radiation damage. It may be defined as the minimum kinetic energy that must be transferred to a lattice atom for it to leave its lattice site and form a stable interstitial. This energy is not only needed to overcome the binding energy but also to move the atom beyond the resulting strain field associated with the vacancy produced to form a stable displaced atom.

Table 2.1

Material	E_d (eV)	Reference
GaAs		
Ga displacements	9.0	23
As displacements	9.4	23
Average	9.2	
Ge	13	24
Si	12.9	25

It is worth mentioning that the experimental technique to evaluate E_d depends, in general, on observation of damage produced by electron bombardment of variable energy[26]. The choice of this technique arises since the electrons penetrate the target deeply and produce uniform damage which may be observed as property changes of the target such as resistivity and minority carrier lifetimes. Also, since electrons have a light mass, simple defects will be produced and hence the property changes can be related directly to the displaced atoms.

Table 2.1 gives values of E_d for Si, Ge and GaAs. Other values have also been reported[27]. A possible reason for the spread in the values reported for E_d may arise from the fact that E_d is a directional quantity and the reported values are averages, the averaging may depend on the particularities of each experiment.

2-5 Band structure

Fig. (2-2) shows a simple energy band structure of GaAs, Ge and Si[29]. The main features of GaAs band structure can be summarized as follows.

The lowest minimum of the conduction band lies in the center of the zone. There are also subsidiary minima that lie away from the zone center. The valence band is similar to that of Ge, with a heavy-hole band and a light hole band. The band is split off by spin-orbit interaction, but this is not shown in Fig. (2-2).

The energy gap of GaAs at room temperature is 1.43 eV which is greater than both Ge (0.66 eV) and Si (1.12 eV).

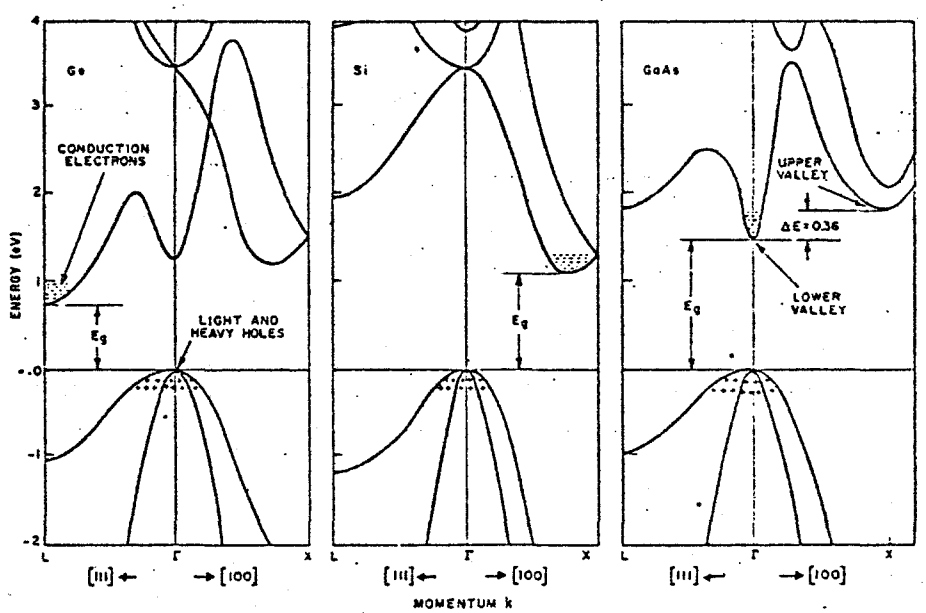

Fig. (2-2) A simple energy band structure of GaAs, Ge and Si. (Ref. 29)

CHAPTER III

ION IMPLANTATION DAMAGE PRODUCTION

3-1 Introduction

An ion implanted into a target loses energy mainly in the excitation of electrons and displacing atoms from their lattice sites. Any displaced atom can, if it has enough energy, produce further displacements leading to a cascade of moving atoms which, when they come to rest, result in a zone of lattice disorder.

A theoretical treatment of elastic and inelastic scattering, cascade production, the number of displaced atoms, and the damage cascade dimensions will be discussed in the following sections.

3-2 Collision Theory

The rigorous description of a "collision" between atoms should be in terms of the superposition of the wave functions of the "colliding" atoms. However, classical mechanics can be used to describe any system if the smallest physical dimension in the system is much larger than the effective wavelength.

In a collision problem, the smallest dimension will be the distance of closest approach in a head on encounter. For mutual Coulomb repulsion, this distance is given classically by;

$$b = Z_1 Z_2 e^2 / E' \qquad (3\text{-}1)$$

where, $Z_1 Z_2$ are the atomic numbers of the interacting particles,

E' is the energy of the incident particle in COM system.

The effective wave length, λ, may be given by,

$$\lambda = h/\left(\frac{M_1 M_2}{M_1 + M_2} v\right) \qquad (3\text{-}2)$$

where, M_1 and M_2 are the masses of the incident and target atoms respectively.

v is the velocity of the incident particle.

An estimation of order of magnitudes for ion implantation system gives

$$b \sim 10^{-10} \text{ m.}$$

and

$$\lambda \sim 10^{-14} \text{ m.}$$

Hence, we may conclude that it is adequate to use classical mechanics for the present purposes.

There are other assumptions involved in the collision theory: the collision is assumed to be binary, and the struck atom is assumed to be stationary before the collision. Also, it is assumed that the incident ion loses its energy through two mechanisms; elastic and inelastic scattering. The two mechanisms are assumed to be independent[30].

3-2-1 Elastic scattering

Fig. (3.1) shows the main features of elastic scattering in both lab and center of mass coordinate systems.

The scattering angle is given by[31];

$$\theta = \pi - 2p \int_0^{u_0} \frac{du}{[1-V(u)/E' - p^2u^2]^{1/2}} \qquad (3.4)$$

where, p = the impact parameter

$E' = M_2E/(M_1+M_2)$

$u = 1/r$, $u_0 = 1/r_0$

r_0 = distance of closest approach

$V(u)$ = the interaction potential

E = the incident particle energy.

In order to evaluate the scattering angle, and hence energy transfers, the interaction potential V(u) has to be specified.

Eq. (3.4) has been evaluated in closed form only for few distinct forms of interaction potentials, for example;

i) Bohr[32] and Rutherford[33] considered the Coulomb potential $V(r) = Z_1Z_2e^2/r$.

ii) The inverse square potential $V(r) = c/r^2$ was considered by Lindhard[34].

iii) Hard sphere potential

$V(r) = 0$ for $r > R$

$V(r) = \infty$ for $r < R$

R = sphere radius

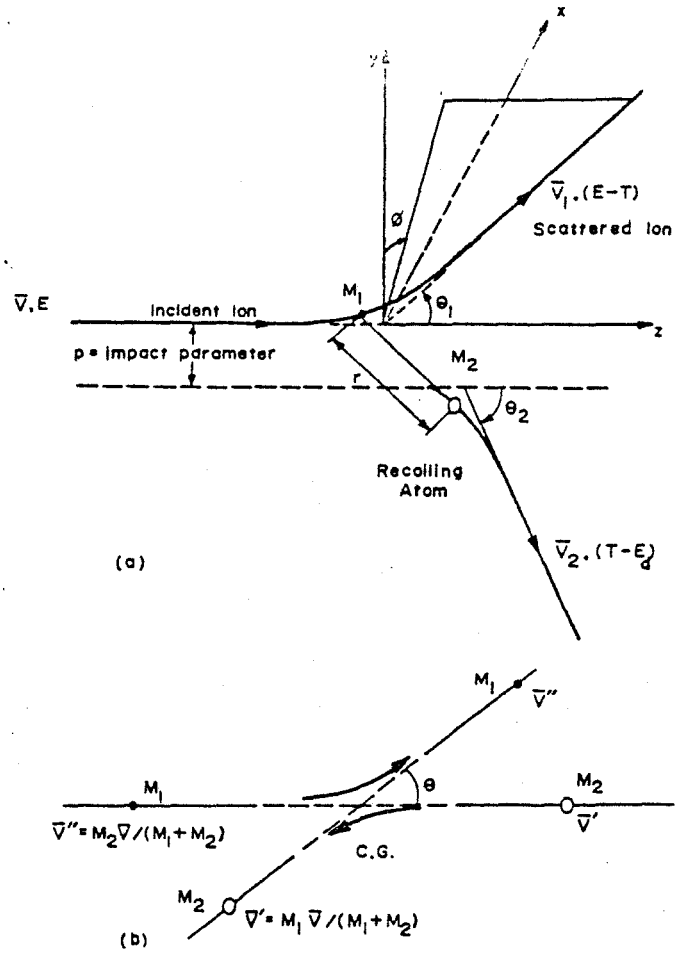

Fig. (3-1) (a) Binary collision in Laboratory Coordinate System

(b) Binary collision in COM Coordinate System.

was also considered[35].

However, in order to evaluate the form of the scattering law, which is essential for ion bombardment problems, it is necessary to evaluate equation (3.4) for a "realistic" interatomic potential.

3-2-2 The interatomic potential

The interaction between the incident ion and target atom is not of pure Coulombic nature because the electrons around the nuclei screen their charges to an extent that depends on the distance of approach.

A number of approximate potentials have been suggested to treat a particular range of approach distance r. For $r \lesssim d$, the Born-Mayer potential[36] can be used. It has the form,

$$V(r) = A\, e^{-Br} \qquad (3\text{-}5)$$

where A and B are constants.

For $r \ll d$, potentials due to Bohr[32], Oen[37], Molière[38], Abrahamson[39-41] and Lindhard[42] have been proposed. Firsov[43] has suggested one convenient potential having a sufficient range of validity to describe the interaction appropriate to ion implantation; it has the form

$$V(r) = \frac{Z_1 Z_2 e^2}{r}\, \phi(Z_1/Z_2, r/a) \qquad (3\text{-}6)$$

where, ϕ is the Thomas-Fermi function which has been calculated by Gombas[44]

and a is the Thomas-Fermi screening length;

$$a = 0.8853\ a_0\ Z_2^{-1/3} \tag{3-7}$$

a_0 being the first Bohr orbital radius for the hydrogen atom. Eq. (3-4) has been solved by perturbation for small angle scattering and the results extrapolated to large scattering angles[45].

Accordingly, the scattering cross-section can be expressed for all combinations of ion and target atoms by[45],

$$d\sigma_n = \frac{1}{2}\,\pi a^2 t^{-3/2} f(t^{1/2})\,dt \tag{3-8}$$

where, the parameter t is given by

$$t = \varepsilon^2 T/T_m \tag{3-9}$$

ε being a dimensionless parameter known as the reduced energy and is defined by

$$\varepsilon = a/b \tag{3-10}$$

T is the recoiling atom energy and T_m is the maximum recoiling atom energy.

The function, $f(t^{1/2})$, is a universal screening function, which can be calculated numerically using the Thomas-Fermi treatment. A convenient approximation to $f(t^{1/2})$ is known as the power cross-section approximation and is expressed as[45];

$$f(t^{1/2}) = \lambda_m t^{1/2-m} \tag{3-11}$$

where

$$0 \leq m \leq 1\ .$$

The values of m for best approximation are chosen according to the value of ε;

For $\varepsilon \geq 10$, $m = 1$, $\lambda_m = 0.5$, this corresponds to Coulombic scattering.

For $0.1 \lesssim \varepsilon \lesssim 2$, $m = \frac{1}{2}$, $\lambda_m = 0.328$, this corresponds to inverse square potential.

For $\varepsilon \lesssim .2$, $m = \frac{1}{3}$, $\lambda_m = 1.309$, this corresponds to an inverse cube potential.

For $\varepsilon << 0.01$, $m = 0$, $\lambda_m = 24$, this approximates the Born-Mayer potential.

The stopping power due to nuclear scattering, $(\frac{dE}{dx})_n$, can then be found as follows:

$$E_{av} = - N\Delta x \int_0^{T_m} T d\sigma$$

where E_{av} = the average energy loss per collision

and N is the atomic density of the target.

As $\Delta x \to 0$, we get the stopping power $\frac{dE}{dx}$;

$$(\frac{dE}{dx})_n = - N \int_0^{T_m} T d\sigma$$

$$= - N \int_0^{\varepsilon} T \frac{\pi a^2 dt}{2t^{3/2}} f(t^{1/2}) \quad .$$

Hence,

$$\left(\frac{dE}{dx}\right)_n = - \frac{N\pi a^2 T_m}{\varepsilon^2} \int_0^{\varepsilon} d(t^{1/2}) f(t^{1/2}) \quad . \tag{3-12}$$

It was found useful to define a dimensionless range parameter, ρ [46];

$$\rho = R\pi a^2 N[M_1 M_2/(M_1+M_2)^2] \tag{3-13}$$

R being the range of the incident ion in the target material. Then, a universal nuclear stopping cross-section, $s(\varepsilon)$, results;

$$s_n(\varepsilon) = - \left(\frac{d\varepsilon}{d\rho}\right)_n = \frac{1}{\varepsilon} \int_0^{\varepsilon} f(t^{1/2}) d(t^{1/2}) \quad . \tag{3-14}$$

For the power cross-section approximation, eqn. (3-14) becomes;

$$s_n(\varepsilon) = \lambda_m t^{1-2m}/2(1-m) \quad . \tag{3-15}$$

For $m = 1$, $s_n(\varepsilon) = \frac{1}{2\varepsilon} \ell n(1.294\varepsilon)$,

for $m = \frac{1}{2}$, $s_n(\varepsilon) = 0.327$,

for $m = \frac{1}{3}$, $s_n(\varepsilon) = 0.981\ \varepsilon^{1/3}$, and

for $m = 24$, $s_n(\varepsilon) = 12\ \varepsilon$.

3-2-3 Inelastic Scattering

In this type of scattering the loss of energy from the incident atom to the target atoms is due to excitation and ionization of the struck atom. This interaction is dependent on the projectile velocity relative to $v_0 Z_1$, v_0

being the orbital velocity of hydrogen atom electrons.

i) If $v_1 >> v_0 Z_1$

In this range, the electronic stopping power is given by[47];

$$\left(\frac{dE}{dx}\right)_e = NZ_2[4\pi(Z_1e^2)^2/m_e v_1^2]L \qquad (3\text{-}16)$$

where, $L = \ell n(2m_e v_1^2/I)$

and $I = I_0 Z_3$ & $I_0 \simeq 10$ eV.

ii) At low velocities $v_1 << v_0 Z_1$

Lindhard[48] and his colleagues have derived an expression for inelastic energy loss where they treated the incident particle as a positive charge Z_1e which loses energy by close collisions with electrons and by collective electron plasma resonance processes in the free electron gas for more distant collisions.

This treatment gives;

$$\frac{1}{N} \cdot \frac{dE}{dx} = S(E) = \xi_e 8\pi e^2 a_0 \frac{Z_1 Z_2}{Z} \frac{v}{v_0} \qquad (3\text{-}17)$$

where, $Z^{2/3} = Z_1^{2/3} + Z_2^{2/3}$

and $\xi_e \simeq Z_1^{1/6}$.

In dimensionless parameters, eq. (3-17) becomes

$$-\left(\frac{d\varepsilon}{d\rho}\right) = s(\varepsilon) = K\varepsilon^{1/2} \qquad (3\text{-}18)$$

where

$$K = \xi_e \frac{0.0793\ Z_1^{1/2} Z_2^{1/2} (M_1+M_2)^{3/2}}{(Z_1^{2/3}+Z_2^{2/3})^{3/4} M_1^{3/2} M_2^{1/2}} \quad .$$

Since $K = K(M_1, M_2, Z_1, Z_2)$, there is no universal curve for $s(\varepsilon)$. Fig. (3-2) shows $s_e(\varepsilon)$ for selected values of K.

An alternative derivation of the inelastic energy loss was developed by Firsov[49] who assumed that electrons from the moving atom lose momentum by transferring to the initially stationary target atom and those from the struck atom gain momentum when transferred to the initially moving particle. These momentum exchange processes occur at the expense of energy loss from the incident particle. The expression he obtained is;

$$-\frac{1}{N}\frac{dE}{dx} = S(E) = 2.34\times10^{-21}(Z_1+Z_2)E_0^{1/2} \text{ ev/m} \quad . \qquad (3\text{-}19)$$

The difference between the Firsov and Lindhard results is not more than about a factor of two. It is important to note that both Firsov and Lindhard treatments predict a monotonic dependence of the energy loss rate upon the atomic number of the incident particle. However, experimental results[50,51] do not support these predictions. The inelastic energy loss of ions in several target materials has shown a periodic dependence on the atomic number of the ion. The monotonic dependence of $\left(\frac{dE}{dx}\right)_e$ on Z_1 arises due to the fact that the atomic

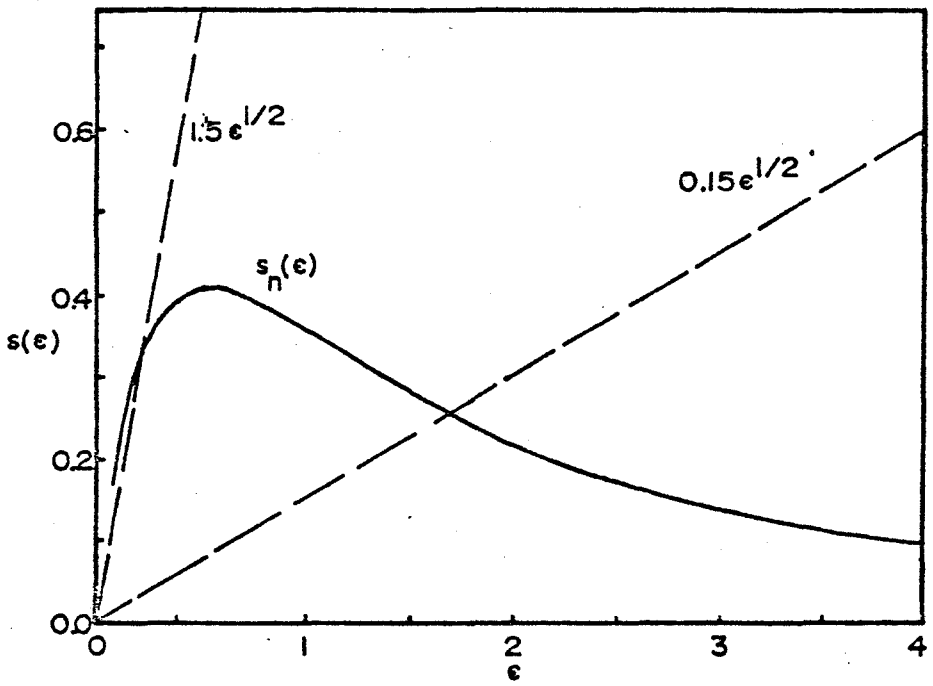

Fig. (3-2) Nuclear and electronic stopping powers in reduced units. (Ref. 48)

charge distributions and potentials are smoothed as a function of atomic radius. More recent theories[52-54] of inelastic energy loss have treated the atoms in terms of their more precise radial electron density wave functions, and these lead to qualitative agreement with the experimental data. The position of the maxima and minima of energy loss oscillation as function of atomic number are reproduced[54] but the magnitudes are not in agreement with the experimental data.

In spite of the oscillatory behaviour, Lindhard's theory is adequate as a first order approximation.

Now we can evaluate the total stopping power $(\frac{dE}{dx})$ from;

$$(\frac{dE}{dx}) = (\frac{dE}{dx})_n + (\frac{dE}{dx})_e \quad . \tag{3-20}$$

At low energies, as shown in fig. (3-2), the nuclear stopping will dominate. The effect of $(\frac{dE}{dx})_e$ on the total $(\frac{dE}{dx})$ will be negligible. For compound targets, such as GaAs, Bragg and Kleeman postulated that[55]

$$S(E)_{molecule} = pS_1(E) + qS_2(E) \tag{3-21}$$

where p/q is the ratio of type (1) to type (2) atoms. Hence,

$$S(E)_{atom} = \frac{pS_1(E)+qS_2(E)}{p+q} \quad . \tag{3-22}$$

3-3 The number of displaced atoms

One of the most important parameters in the study of ion implantation is the number of displaced atoms that results from the collision cascade. A simple model has been proposed by Kinchin and Pease[56], who treated the collision as a two body event and assumed a threshold displacement energy E_d such that, if an atom receives energy less than E_d it will not be permanently displaced. This model gives the number of displaced atoms as;

$$N_{kp} = E/2E_d \ ; \text{ for } E > E_d \qquad (3\text{-}23)$$

where E is the incident ion energy. An upper energy, E_A, for the validity of this approximation can be found from the condition that the projectile and the target nuclei are separated by the sum of the radii of their screening clouds. This gives;

$$E_A = 27.2\ Z_1 Z_2 (Z_1^{2/3}+Z_2^{2/3})^{1/2}(M_1+M_2)/M_1 \ [ev] \ .$$

This model has been modified by Robinson[57,58]. He generalized the assumptions to allow for inelastic and elastic collisions with screened Coulomb potential. So eq. (2-23) becomes;

$$N = \xi(m)\nu \cdot E/2E_d \qquad (3\text{-}24)$$

where, ν is the fraction of energy deposited into elastic collision events.

The fraction of energy loss into inelastic events is given as η, where $\nu+\eta = 1$, and

$$\xi(m) = 2(2^m-1)/[\psi(1)-\psi(1-m)]$$

and

$$\psi(x) = \frac{d}{dx} \ell n\Gamma(x) \ .$$

Sigmund[59] has suggested that $m = 0$ approximation should be used since it is the number of near threshold collisions ($E \sim 2\ E_d$) of the higher generation of recoil atoms, which primarily determines N(E) and hence m. This leads to;

$$N(E) = \frac{6}{\pi^2} \nu \cdot \frac{E}{U} \ell n(1+U/E_d) \qquad (3\text{-}25)$$

where, U is the binding energy. For semiconductors, the displacement energy will be approximately four times the bond energy, and accordingly, for $U = E_d$;

$$N(E) = 0.42\ \nu \cdot E/E_d \ . \qquad (3\text{-}26)$$

This equation is similar to eq. (3-23) and referred to as the modified Kinchin Pease equation.

3-4 Cascade dimensions

The cascade dimensions depend on the spatial distribution of the elastic energy deposition. In order to find the equation governing the energy deposition[46], we assume an ion with velocity $\bar{v}$ striking the target surface at $\bar{r} = 0$. The energy deposited in a volume d^3r at $\bar{r}$ is given by $F(\bar{r},\bar{v})d^3r$.

The probability for a collision to occur when particle moves a distance $\overline{\delta R}$ is $N\overline{\delta R}\, d\sigma$, where $d\sigma$ is the scattering cross-section and N is the atomic density, the corresponding deposited energy will be

$$N\ \overline{\delta R}\ d\sigma[F(\bar{r},\bar{v}')+F(\bar{r},\bar{v}")]d^3r$$

v', v" being the velocities of ion and recoil. The probability for collision not to occur is $(1-N\overline{\delta R}\ d\sigma)$, leading to deposited energy; $(1-N\overline{\delta R}\ d\sigma)F(\bar{r}-\overline{\delta R},\bar{v})d^3r$. Hence, the total energy deposited $F(\bar{r},\bar{v})$ is

$$F(\bar{r},\bar{v}) = [N\overline{\delta R}\int d\sigma[F(\bar{r},\bar{v}') + F(\bar{r},\bar{v}") + (1-N\overline{\delta R}\int d\sigma)F(\bar{r}-\overline{\delta R},\bar{v})] .$$

This leads to;

$$\frac{\bar{v}}{v}\frac{\partial}{\partial r}F(\bar{r},\bar{v}) = N\int d\sigma[F(\bar{r},\bar{v}")+F(\bar{r},\bar{v}') - F(\bar{r},\bar{v})] . \qquad (3\text{-}27)$$

This is the basic integrodifferential equation for the spatial distribution of energy deposition in its simplest form.

It is impossible to determine analytically the exact form of the deposited energy spatial distribution function. However, multiplication of eq. (3-27) by r^n and integration by parts leads to a recursive expansion for the spatial moments[46,60]. The problem then becomes one of constructing the distribution from a finite number of generated moments

using truncated statistical methods.

The Edgeworth expansion,[61,62] is used for this purpose. It has the advantage of having a simple form and being a weighted-Gaussian function. For incidence normal to the target surface, the longitudinal distribution may be expressed in terms of Edgeworth expansion, for the first four moments, as;

$$F(Z,E) = \frac{\tilde{g}}{\sqrt{2\pi}\ \sqrt{\mu_2}} \exp(-\frac{\xi^2}{2}) f(\xi) \qquad (3\text{-}28)$$

where, $$f(\xi) = 1 - (\frac{\mu_3}{6\mu_2^{3/2}}) \cdot (3\xi - \xi^3)$$

$$+ \frac{1}{24} (\frac{\mu_4}{\mu_2^2} - 3) \cdot (3 - 6\xi^2 + \xi^4)$$

$$- (\frac{\mu_3^2}{72\mu_2^3}) (15 - 45\xi^2 + 15\xi^4 - \xi^6) \ ;$$

and $$\xi = \frac{Z - \langle Z \rangle}{\mu_2^{1/2}}$$

$$\mu_n = \langle (Z - \langle Z \rangle)^n \rangle$$

$\tilde{g}$ = 1 for range

= $\nu \cdot E$ for damage

= ηE for ionization .

Examples of distributions obtained for heavy and light ions incident on Ge (the elemental counter part of GaAs) are shown

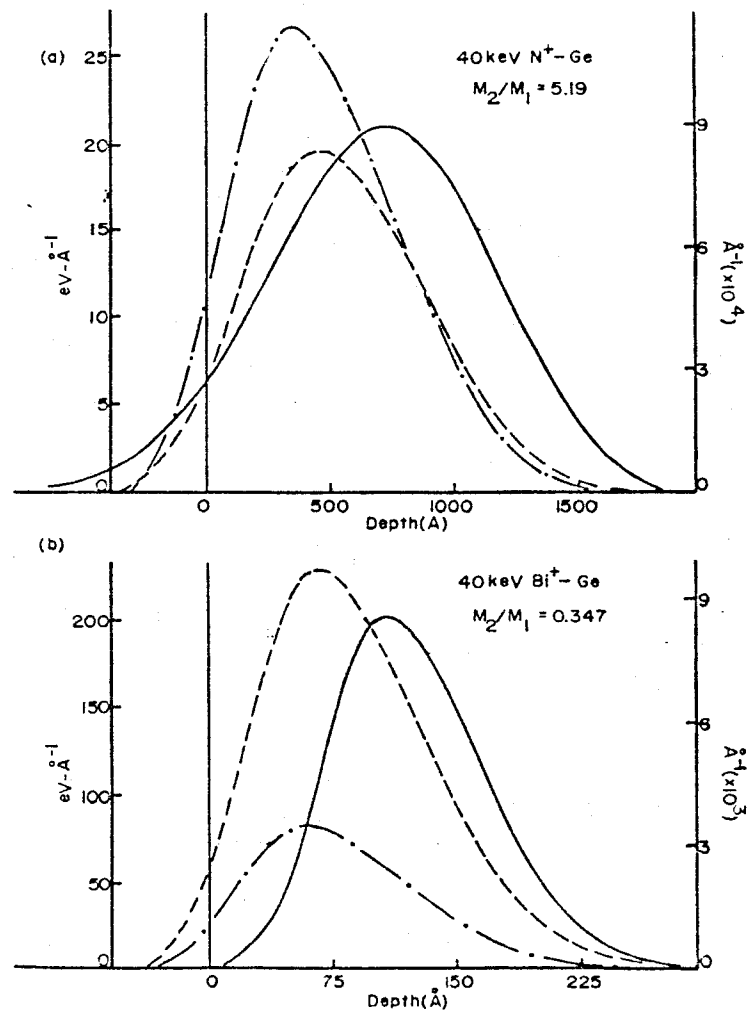

Fig. (3-3) Distributions obtained from Edgeworth series expansion of first four longitudinal moments.

Range, damage and ionization are represented by solid line, dashed line and dot-dash line respectively.

in Fig. (3.3). From this figure, light ions penetrate deeper than heavy ions. The damage profile is similar to the range profile but with the peak at less depth.

3-5 Discussion of the cascade theory

One of the major assumptions of the theory is that the collision occurs between isolated atoms. However, as the collision density becomes higher, atoms interact collectively rather than discretely. Experimental evidence for collective atomic interactions in dense cascades has been reported in studies of sputtering by heavy ions[63,64] and studies of damage production in heavy ion bombarded semiconductors[65-70].

The other basic assumption is that the deposited energy can be divided into two components; elastic and inelastic. The first component is responsible for displacing atoms while the second does not generally contribute to damage production. However, the discrepancy between the theoretically predicted number of displaced atoms and the number obtained experimentally by bombarding semiconductors (and insulators) with energetic light ions, has led to the development of models for defect creation by ionization. However, for heavy incident ions with energies up to a few hundred keV (as used in ion implantation) the fraction of energy into ionization effects is typically 20-50%. This leads to the conclusion that inclusion of the inelastic energy loss could not account for the discrepancies between measured and calculated damage levels. As a result of this discrepancy, spike mechanisms have been proposed.

3-5-1 Defect production by ionization

Before discussing any model for damage production due to the inelastic energy deposition, the physical feasibility of ionization contribution to the displacement process has to be checked.

It is known that any initial non-equilibrium distribution of charge produced by non-ohmic forces, such as radiation, must decay to zero with time constant given by $\tau = \varepsilon/\sigma$, where ε and σ are the permittivity and conductivity of the material respectively. The minority carrier life time, τ_ℓ, is given by:

$$\tau_\ell = (n_c \sigma_t v_{th})^{-1} \qquad (3\text{-}29)$$

where n_c is the concentration of whichever carrier is involved, σ_t the trapping cross-section for this carrier and v_{th} is its effective thermal velocity.

For n_c equal to 10^{17} cm^{-3} and σ_t equal to 10^{-16} cm^2, $\tau_\ell \simeq 10^{-8}$ sec which is a long time (compared to lattice vibrations). Hence, it is reasonable to consider models for ionization mechamisms contributing to atomic displacements. Such models will not be applicable to metals nor to heavily doped semiconductors.

Models for ionization-assisted defect production have been discussed by several authors[71-73]. The basic ideals are;

a) ionizing the outer-shell electrons will weaken the bond and hence reduce E_d. This will result in an increased number of displaced atoms.

b) inner-shell (plus outer-shell) ionization can also contribute to displacement process either alone or in conjunction with elastic energy transfer, by modifying the interaction potential to be more repulsive.

c) a model was suggested that derives its displacement energies from the contribution of the elastic strain surrounding a vacancy created by a standard elastic collision and the ionization of the neighbouring atoms.

d) for high rates of ionization losses, neighbouring atoms will be in mutually repulsive states in which the Coulombic repulsive force may be sufficient to overcome the displacement energy.

3-5-2 Spike mechanism

A) Displacement spike.

Brinkman[74,75] proposed that when the mean free path between displacement collisions approaches the interatomic spacing of the target, a violently disturbed region will be created. In this region, the displaced atoms move outward from the center, and because their energies are low, come to rest at small distances from this center. Hence a vacancy rich core will be created with a surrounding region containing an excess of interstitial atoms.

Heavy ions ($M_1 \gtrsim 100$) with energies in the range $\sim$ 10 to 60 keV would typically result in a displacement spike extending over essentially the total cascade dimensions[76].

Fig. (3-4) shows a schematic representation of the proposed displacement spike.

Since this region of the lattice is greatly disordered, with resulting strains, it may be anticipated that many of the defects produced in the spike will migrate to take up a more energetically favourable configuration. Nevertheless, a certain degree of disorder will persist.

The high concentration of defects may lead to either a thermal collapse of the lattice into an amorphous state or to a thermal spike.

B) Thermal spike

When the primary atom energy degrades to $\lesssim E_d$ it will not be able to produce further displacements, but in order to achieve thermal equilibrium with the lattice, it must dissipate most of this excess kinetic energy as heat or lattice vibrations. This type of dissipation is termed thermal spike[77]. The time required for 10-100 keV ions to come to rest is $\sim 10^{-13}$ sec. If the number of atoms involved in the cascade volume is large enough, typically $\sim 10^4$-10^5 atoms[76], their energy distribution can be described by Maxwell-Boltzmann statistics, i.e. after 10^{-12} sec. The concept of local temperature and heating becomes practical. Brinkman[74] has pointed out that the thermal spike could occur after the propagation of the displacement spike.

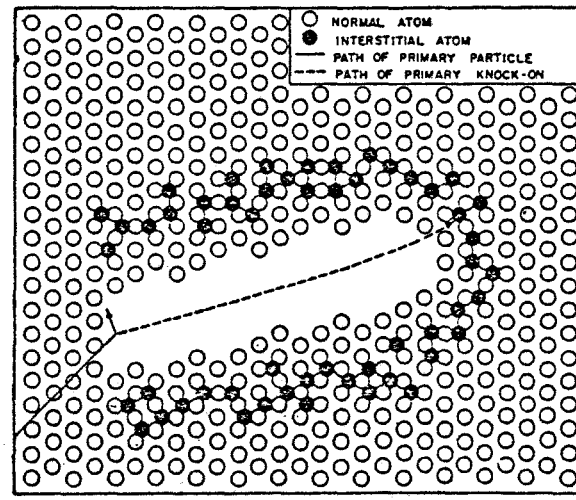

Fig. (3-4) Schematic representation of the displacement spike. (Ref. 74)

Several workers[77-80] have treated the evolution of a thermal spike theoretically. The common assumption in all models is the applicability of the normal heat transport equation;

$$\frac{\partial T}{\partial t} = K \frac{\partial^2 T}{\partial x^2}$$

where, K is the thermal diffusivity.

A difficulty appears in determining the appropriate value of K. The normal thermal conductivity consists of two parts due to lattice and electronic contribution. It was shown[75], however, that the coupling between the lattice and electrons is not sufficiently strong to permit appreciable exchange of energy in times of the order of 10^{-12} sec. Since the times involved in energy spikes are of this magnitude or less, energy given to an atom will be dissipated in the lattice only, i.e., the effective thermal conductivity is the lattice conductivity.

Another model for calculating K has also been suggested, e.g., Sigmund[59] has calculated K from kinetic gas theory assuming that the spike region can be treated as a high pressure gas.

Once a value is assigned to K, the temperature-time evolution of the spike can be determined and the resulting effects, such as defect migration, annealing, etc., can then, in principle, be determined.

CHAPTER IV

RBS-CHANNELING TECHNIQUE AND INSTRUMENTATION

4-1 Introduction

Many techniques have been developed to study the defects introduced in a material as a result of ion bombardment. They can be generally divided into two categories; direct and indirect techniques. Transmission electron microscope[81] and Rutherfor d backscattering combined with channeling[82] are examples of direct techniques of damage measurement. Optical reflectivity[83], optical absorption, electrical conductivity, electron spin resonance, etc. are examples of indirect techniques.

Each of these techniques yields information about different aspects of disorder. For example, optical absorption and ESR[84] measurements give microscopic information about specific defects that must be located in essentially crystalline regions for identification. Optical reflectivity can be used to evaluate the information of the amorphous layer. Electron microscopy gives information about the presence of disordered regions and the growth of dislocations[85]. Channeling effect measurements detect disorder and its depth distribution but do not give information about the microscopic nature of the defects. It is widely used, with regard to ion

implantation of semiconductors, to give a quantitative measure of the damage and damage depth distribution produced.

4.2 Rutherford backscattering-channeling

4-2-1 Rutherford backscattering

When a beam of "monoenergetic" particles strikes the surface of a target, some of the incident particles will be scattered. The likelihood of occurence of a scattering event with an angle θ w.r.t. the incident beam for ion-target system having $\varepsilon T/T_m \gtrsim 100$ is given in COM by[86];

$$(d\sigma/d\Omega)_c = \left[\frac{Z_1 Z_2 e^2}{4E_c \sin^2 \theta_c/2}\right]^2 \qquad (4\text{-}1)$$

where $(\frac{d\sigma}{d\Omega})_c$ is the differential scattering cross-section

θ_c scattering angle

E_c the energy of the incident particle.

Eq. (4-1) can be expressed in the lab frame of reference as[87];

$$\frac{d\sigma}{d\Omega} \simeq \left(\frac{Z_1 Z_2 e^2}{4E}\right)^2 \left[\sin^{-4}\frac{\theta}{2} - 2\left(\frac{M_1}{M_2}\right)^2 + \cdots\right] . \qquad (4\text{-}2)$$

The energy of the scattered particles E_1 is related to the incident energy E by

$$E_1 = \kappa E.$$

κ is called the kinematic factor which expresses the energy lost in the collision process. It can be evaluated by making use of conservation of energy and momentum principles. Then,

we get;

$$\kappa = \{\frac{[1-(M_1/M_2)^2\sin^2\theta]^{1/2}+(M_1/M_2)\cos\theta}{1+(M_1/M_2)}\}^2 \qquad (4\text{-}3)$$

As the particle penetrates the surface and subsequently backscatters at depth, t, it will lose energy before and after scattering. A continuous spectrum of backscattered particles will result for $E < E_1$ where;

$$E(t) = \kappa[E - \int_0^{t/\cos\theta_1} S(E)dt] - \int_{t/\cos\theta_2}^{0} S(E)dt.$$

$$\simeq \kappa E - t[KS(E)+S(E_1)/|\cos\theta|] \qquad (4\text{-}5)$$

where S(E) is assumed constant over the limits of integration. The correspondence between incremental energy ΔE and incremental depth Δt will then be,

$$\Delta t = \Delta E/[\kappa S(E)+S(E_1)/|\cos\theta|] = \Delta E/S_{av} . \qquad (4\text{-}6)$$

4-2-2 Channeling

The backscattering from a single crystal is a direction dependent phenomenon. If the direction of a particle incident upon the surface of a crystal lies close to a major crystal direction, it will suffer a series of correlated, small angle deflections as it passes by neighbouring atoms in the same row. The ion is said to be channeled and a reduction in the back-

scatter occurs. In general, for a particle incicent with an angle ϕ to the major axis, there will be three distinct trajectories that the incident particle may have[89];

a) For $\phi \lesssim \psi_c$, the ion follows a channeled trajectory. ψ_c is a critical angle given by;

$$\psi_c = \left(\frac{2Z_1Z_2e^2}{E \cdot d}\right)^{1/2} \qquad (4\text{-}7)$$

where d is the distance between adjacent atoms along the chosen atomic row.

b) For $\phi >> \psi_c$, the correlated small angle scattering can not occur, and the ion will follow trajectory c (in fig. 4-1-a). This trajectory is referred to as random, although the use of the term in connection with a crystal may be vague.

c) For ϕ only slightly greater than ψ_c, the ion spends more time near the lattice row with the consequence of enhanced probability of collisions. The ion is then said to be quasi-channeled.

Fig. (4-1-a) shows the three basic trajectories and fig. (4-1-b) shows the correspondence between the backscatter yield and the angle of incidence. The angular yield can be described mainly by two quantities[82]; the normalized minimum yield, χ_{min}, which is the ratio between the aligned yield and the unaligned (random) yield near the surface, and the half-width, $\psi_{1/2}$, which is taken at $\frac{1}{2}(1 + \chi_{min})$. These two quan-

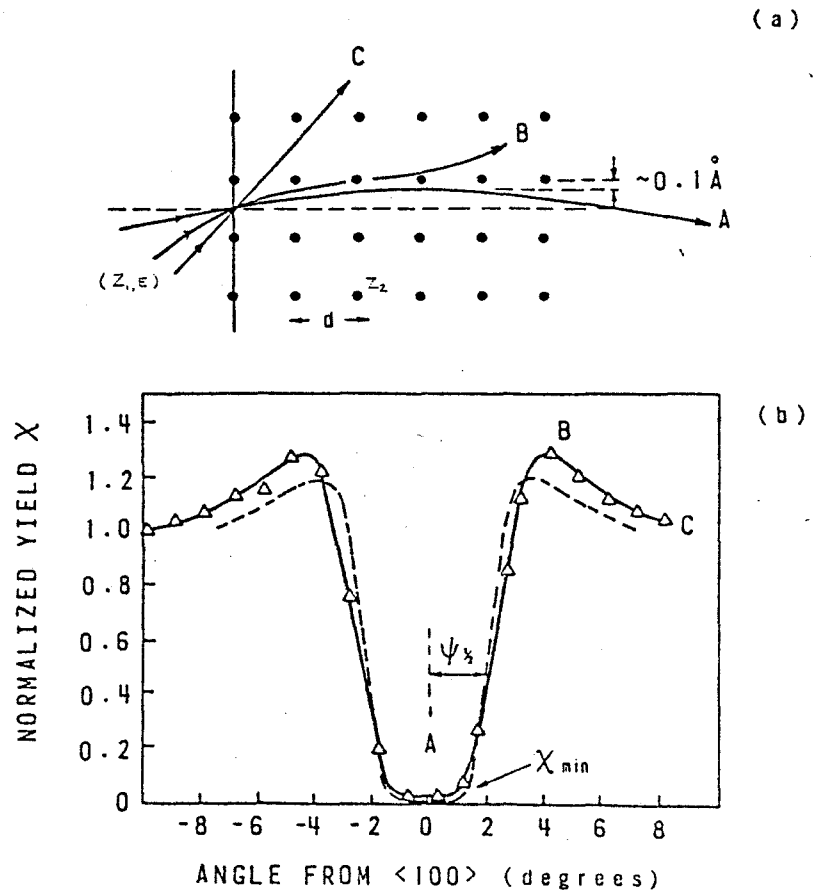

Fig. (4-1) (a) Ion trajectories for three typical values of the angle, ϕ, between the incident beam and the lattice row.

(b) The relation between the back-scatter yield and the angle ϕ.

(Ref. 89)

tities can be estimated from values of the Thomas-Fermi screening radius, thermal vibrational amplitude and other crystal parameters. Differences between theoretical and experimental χ_{min} appear due to the influence of factors like contamination, lattice strain, beam divergence, etc.

Fig. (4-2) shows backscattering spectrum of 1 MeV $^4He^+$ from Si target for aligned and non-aligned incidence of helium ions. Also, the corresponding angular scan is shown.

The main features of the non-aligned spectrum are;

a) Sharp edge corresponding to $K_{Si}E$.

b) Increase in the yield as the energy decreases because of the increase of the scattering cross-section ($\propto E^{-2}$).

The main features of the aligned spectrum are;

a) A decrease in the yield. However, it does not go to zero because there is no complete shadowing of atoms in a row. At lower temperatures atomic vibration will be less and hence a lower yield may be obtained.

b) A peak appears that corresponds to scattering from the surface of the crystal partly because surface atoms are not shadowed and partly because of crystal surface imperfections.

c) Increase in the yield as the energy decreases which is a result of the beam being dechanneled as it penetrates deeper in the crystal and because of the increase in the scattering cross-section.

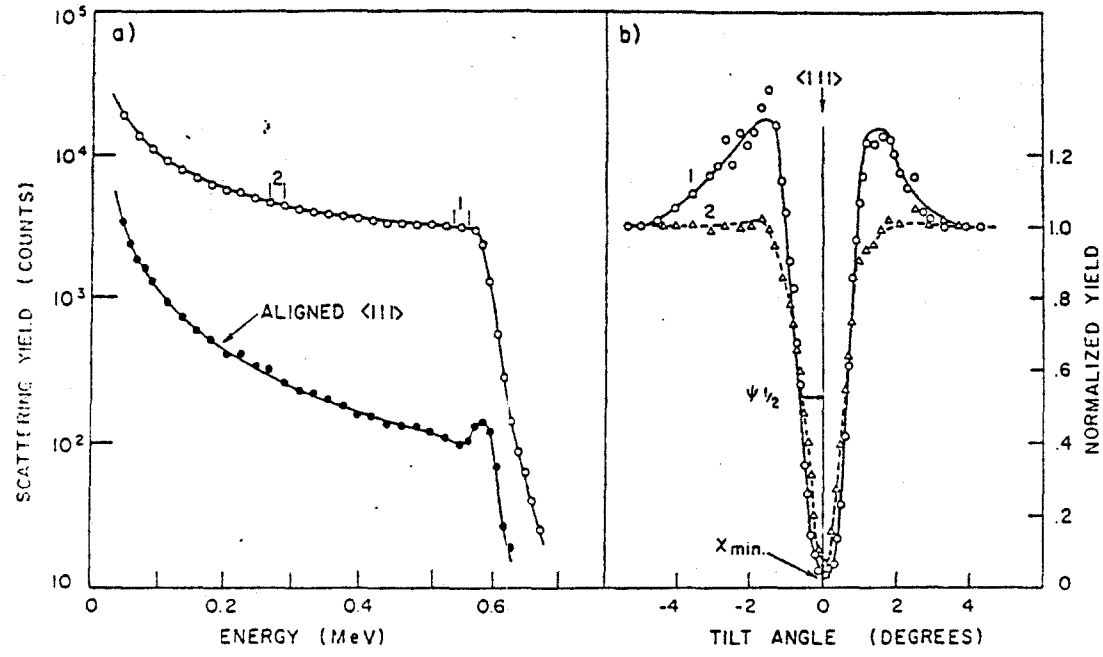

Fig. (4-2) The backscatter spectrum of 1 Mev $^{4}He^{+}$ from Si target for aligned and non aligned incidence of He ions. (Ref. 89)

4-3 Analysis of Damage by RBS-channeling

When the crystal is irradiated, a number of lattice atoms will be displaced from their sites, and act as scattering centers. This will lead to an increase in the surface peak of the backscatter spectrum. The yield behind the surface peak will also be higher because on passing through a damaged layer, a larger fraction of the He beam becomes dechanneled due to scattering of the He ions by the lattice atoms.

Fig. (4.3) shows the backscatter spectra due to aligned beam incident on an undamaged and damaged (irradiated) crystals. Also the spectrum due to non-aligned incidence is shown.

The analytical procedure by which the backscatter peak is related to the damage is based on the assumption that at some depth, t, below the crystal surface, the incident aligned beam consists of an aligned and a random component. This leads to the relation[82];

$$y'(t) = y_R(t)\left[\{1-\chi'(t)\}\frac{N'(t)}{N} + \chi'(t)\right] \qquad (4\text{-}8)$$

where, $y'(t)$ is the backscattered yield from depth t, y_R is the yield with the beam incident in a non-aligned direction, χ' is the non-aligned fraction of the analysing beam $N'(t)$ is the density of displaced atoms at depth t, and N is the atomic density of the crystal.

The first term on the right is due to the scattering of channeled ions from scattering centers and the second is due to the scattering of the non-aligned portion of the beam. This equation neglects the possible difference in the scattering cross-section for the aligned and random beams at a given depth. Eq. (4-8) can be solved for N'(t) to give;

$$N'(t) = N \frac{\{[y'(t)/y_R(t) - \chi'(t)\}}{\{1-\chi'(t)\}} \quad . \qquad (4\text{-}9)$$

If we divide the energy scale in channels of width ΔE, there will be correspondence between depth, t, and channel, i, eq. (4-9) can then be written as

$$N'(i) = N \frac{\{[y'(i)/y_R(i)] - \chi'(i)\}}{(1-\chi'(i))} \quad . \qquad (4\text{-}10)$$

The total number of displaced atoms, N_D, will be given by summation over the surface peak width. In order to do that $\chi'(i)$ (or equivalently $\chi'(t)$)has to be defined. This dechanneling function has to satisfy the following conditions;

a) the damage returns to zero beyond the damage layer

b) it should merge smoothly with the dechanneling beyond the damage layer

c) the dechanneling at the surface should be zero.

Different models[90,91] have been proposed for dechanneling that satisfy the above conditions.

Linear dechanneling, as shown in fig. (4-3), is a simple

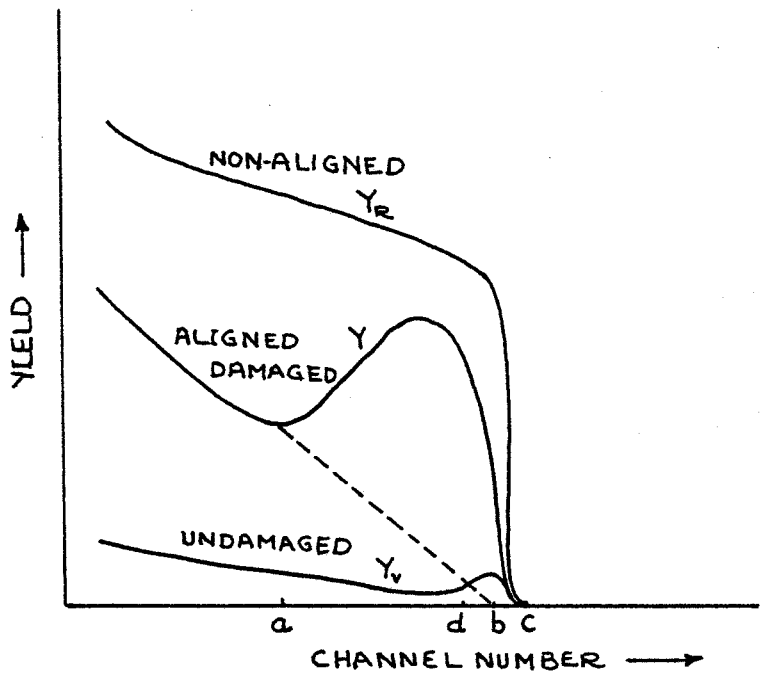

Fig.(4-3) Schematics of non-aligned, aligned undamaged and aligned damaged backscatter spectra.

and widely accepted model, however it does not satisfy condition (b) in general. The difference of results obtained using this model agree within 5% of the results obtained using more complicated models which involve calculating the dechanneling based on single or multiple scattering processes. Accordingly eq. (4-10) gives;

$$N_D = \frac{N\Delta E\{\sum_{k=a}^{c} y(k) - \frac{1}{2}(b-a+1)y(a) - [\sum_{d}^{c} y_v(k) - \frac{1}{2}(y_v(d)\cdot(b-d+1)]}{S_{AV}\{y_R - \frac{1}{2}[y(a) + y_v(b)]\}} \qquad (4\text{-}15)$$

where, points a, b and c are as defined in Fig. (4-3),

y_v is the undamaged yield

S_{AV} is defined by eq. (4-6).

4-4 Discussion of the technique

One of the major advantages of RBS technique using light ions (e.g. H^+, He^+) at MeV energies is that, the cross sections are accurately predictable and thus calibration procedures are not necessary[88]. Also, it provides depth information ($\lesssim$ 1 μm) without destruction of the sample as some other methods do, e.g., the radiotracer method.

However, this technique has its limitations. It requires a well-resolved backscatter peak for the analysis described in the previous section to be possible. For metals, there is no damage peak[92] and even in semiconductors there is a lower limit on the amount of disorder that can be measured which is determined by the quality of the crystal as re-

vealed by χ_{min} and the rate of dechanneling. The sensitivity can be increased by double alignment of the crystal. This requires both the incident and detected beams to be aligned simultaneously with major crystal axes, or planes[89].

In a comment on measurement of radiation damage by RBS experiments, Quéré[93] has explained that at high implanted ion doses, the technique indicates only the relative lattice disorder and one should be careful in interpreting the values of N_D quantitatively.

A potentially important factor that has to be fully understood, is the influence of the probing beam on the measured damage because it does and can under certain circumstances cause annealing of damage. In the previous section it was implicitly assumed that the channeled beam is uniformly distributed over the channel, however, it has been shown[94,95] that in a well-ordered crystal, the channeled beam is rather focussed near the middle of the channel. Accordingly, an enhancement in the backscatter yield from an interstitial near the middle of the channel is expected. However, flux peaking is not expected to affect the measurements of randomly distributed atoms in the channel. On the other hand, flux peaking should be less pronounced as the number of scattering centers increase, i.e. the presence of defects works to destroy flux peaking. It is also

important to note that; in order to accommodate the radiation induced defects, lattice atoms may relax $\geq$ 0.1 Å into the channel with the consequence of an increase in the dechanneling. Also, direct backscattering can occur when the relaxations are large enough.

4-5 Instrumentation

In this section a short description of the experimental apparatus and procedures will be outlined. This includes, the description of a coupled accelerator system, which enables in situ measurement of damage, data handling, and the major factors considered for selecting the various experimental parameters.

4-5-1 Accelerator, Beam Transport and Sample Manipulation

A coupled accelerator system has been used for implantation and analysis; it is shown schematically in Fig. (4-4). It consists mainly of; a 150 kV-ion accelerator using a DANFYSIK 911 A "universal" ion source suitable for producing ions from gas and solid sources, and a 3.5 MeV Van de Graff accelerator used to obtain the analysing He-beam. This beam is collimated to 0.037° half angular divergence using two 0.75 mm diameter apertures. The beam from either accelerator may be directed onto the target via a common analysing magnet. A feedback circuitry is used for stabilizing the energy of the beam.

During implantation, the ion is swept vertically and

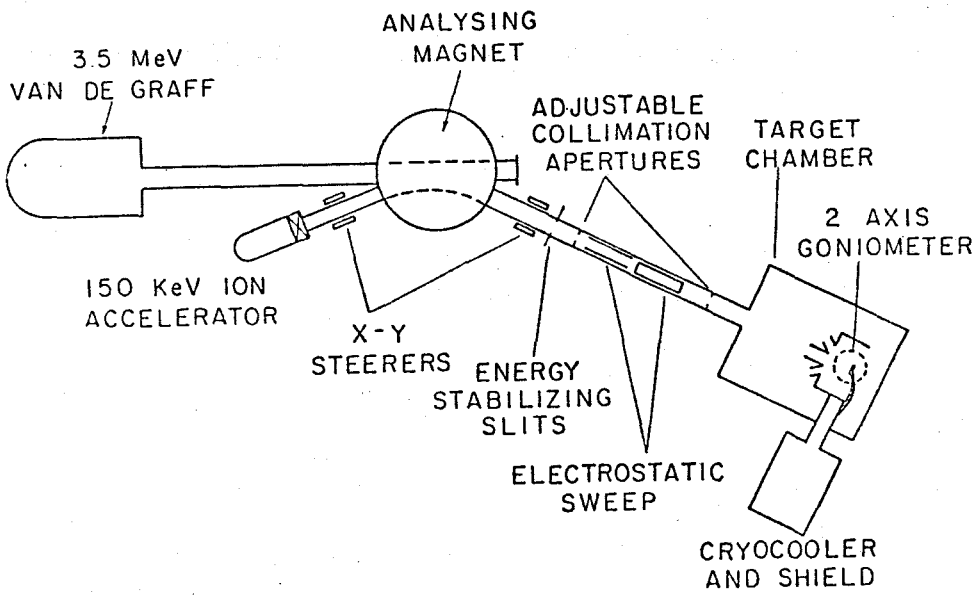

Fig. (4-4) Schematic of the coupled accelerator system.

horizontally to ensure the uniformity of the implantations. Also, the beam defining apertures are adjusted to 2 mm and 4 mm. The 2 mm is placed usually off axis vertically so that there is no direct path from the magnet to the target. Electrostatic deflecting plates are then employed to direct the beam to the target. This ensures that ions neutralized between the magnet and beam sweep will not strike the target.

The target is mounted on a goniometer that has two degrees of rotation so that the target can be rotated and tilted w.r.t. the incident beam. The goniometer is placed in a vacuum chamber with base pressure of $\sim 10^{-6}$ Torr. A cryocooler is attached to the target via a flexible copper braid to the target mount which is surrounded by a copper shield that is also attached to the cryocooler. This target-shield arrangement acts as a Faraday cup for beam current measurements. The target mount is thermally isolated using a thin wall stainless steel tube. The target temperature can be lowered to $\sim$ 40 K. A gold (doped with 0.07 % Fe) - chromel thermocouple is fixed to the copper target mount to measure the target temperature. A radiation shield in the chamber surrounds the cryocooler to minimize the radiative heat load. Another radiation shield, directly cooled by a flow of liquid nitrogen, encloses the greater part of the inner shield. A schematic diagram of the chamber is shown in fig. 4-5. The target mount is thermally isolated using a thin wall stainless steel tube.

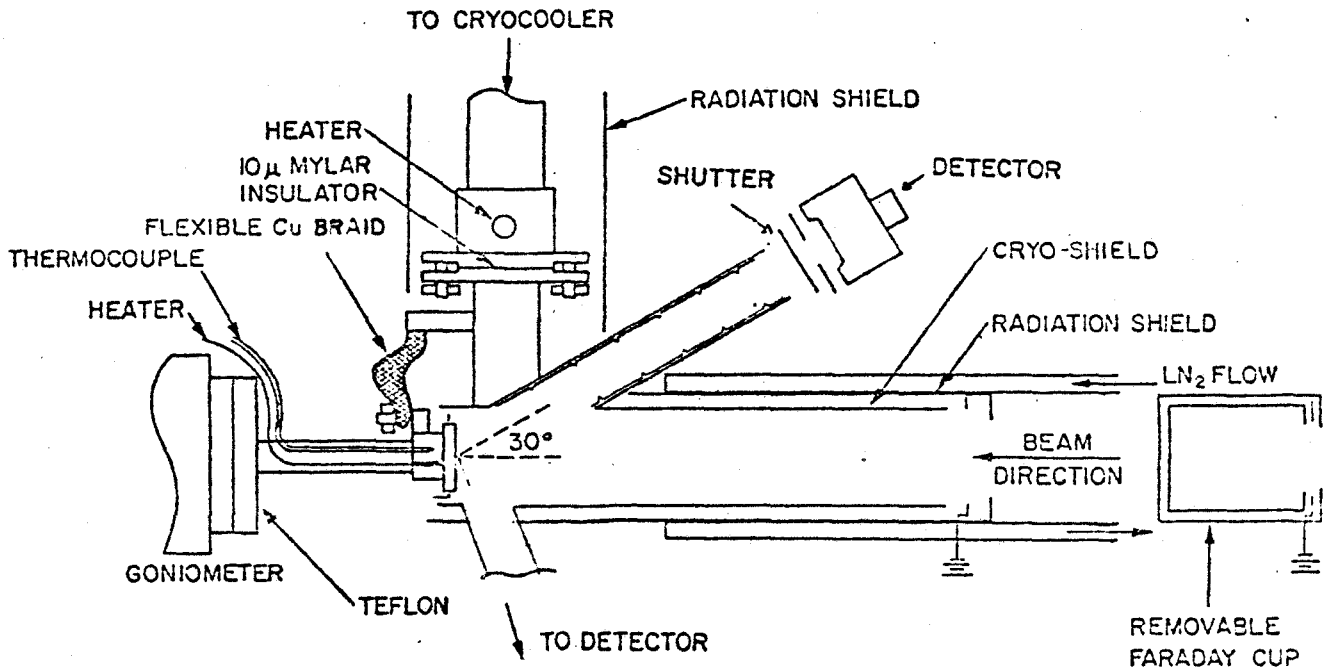

Fig. (4-5) Schematic of the target chamber.

REPEATED

A radiation shield in the chamber surrounds the cryocooler to minimize the radiative heat load. Another radiation shield, directly cooled by a flow of liquid nitrogen, encloses the greater part of the inner shield.

5-4-2 Data Handling

The implant dose is determined by measuring the integrated charge at the target over the period of the implant. To ensure accurate measurement of current, the target mount and the copper shield are electrically isolated from the cryocooler by a 10 μ Mylar film and from the goniometer by a Teflon washer. Secondary electrons are suppressed by applying -100 v to suppression rings which are placed at the shield where the beam enters.

The backscattered He particles are detected by a silicon surface barrier detector (FWHM ∿ 15 kev) which is mounted at an angle 150°. The detector solid angle is .0375 str.

A PDP 11/05 minicomputer is incorporated to perform pulse-height analysis and data processing.

A current digitizer (Ortec model 439) measures the beam current at the target or Faraday cup. This digitizer can feed an Ortec model 771 timer/scaler which also acts as a control unit for data acquisition.

5-4-3 Experimental Parameters

The shape of the backscattering spectrum depends on the choice of beam parameters. Since the scattering cross-section is inversely proportional to the square of the energy, better statistics are expected at lower energies. However, the cross-section of damage production by the analysing beam has similar energy dependence, so a lower energy helium-beam induces more damage. Another factor considered for selecting beam energy is the mass resolution. However, since Ga and As have masses that have value near each other, unconvoluted peaks will not be obtainable for energies typical to RBS analysis due to the limited resolution of the detector.

The beam energy used throughout all the experiments reported here is 2 MeV.

A beam current of $\sim$ 10 nA/mm^2 was used, so that the "deadtime" (difference between the actual counts and the number counted by the analyser) was not more than $\sim$ 1%. The integrated beam currents were typically 2 μC, this value represents a compromise between good statistics and beam induced damage effects.

CHAPTER V

DAMAGE PRODUCTION BY 2 MeV $^4He^+$ IN GaAs AT 40 K

5-1 Introduction

In chapter IV, the RBS-channeling technique was presented and it was indicated that helium beam probe could have an influence on the measured damage. In general, He-beam produces damage. This damage is frozen-in and observable at low temperature, while at room temperature, the observed damaging effect will be less due to the existence of annealing. However, if the beam current is high enough, it can produce local heating with the consequence of annealing the original damage. This may occur, even in a low temperature experiment. This chapter reports on the investigation of damage induced by 2 MeV helium in GaAs and its dependence on previous heavy ion damage.

The problem of introducing damage by helium beam bombardment in Si has been investigated by a number of workers. Pabst et al.[96] have reported on the damage introduced in unimplanted Si crystals by non-channeled 275 keV $^4He^+$ irradiation at 300 K. Also, the damage produced by 100 keV and 200 keV $^4He^+$ bombardment has been reported[97,98]. In all these cases the damage produced was in excess of the theoretical predic-

tions. The dependence of disorder production rate on temperature and alignment has been studied by Thompson et al.[10] where 1 MeV $^4He^+$ has been used to bombard unimplanted Si crystals in aligned and non-aligned directions at 40 K and 300 K. The disorder production rate was found to be weakly dependent on temperature and alignment.

The effect of helium beam on implanted Si has also been investigated; Haskell et al.[99] have reported on the effect of 1.8 MeV $^4He^+$ bombardment of As-implanted Si. The initial displacement rate of As was found to be independent of As concentration. They concluded that the displacement can not be due to direct impact of the impinging beam particles on the impurities but must be attributed to the interaction of the impurity atoms and primary defects produced by the beam particles. Kool et al.[101] have investigated the bulk and surface damage produced by 200 keV He^+ beam bombardment of both unimplanted and As-doped Si samples. They concluded that the damage production cross-section is at least five times that expected from theory. Eisen et al.[100] have studied the effect of 400 keV $^4He^+$ on As-implanted Si and suggested that the movement of As off lattice sites is caused by the production of defects which are able to diffuse over larger distances towards the surface region.

The temperature dependence of the displacement of As atoms in Si at temperatures in the range 40-720 K due to 1-2

MeV He^+ bombardment has been reported by Swanson et al.[102]. They found that the initial displacement rate as well as the saturation value increased gradually at higher temperatures until 423 K after which there was a decrease in displacement rate.

More recently, Wiggers et al.[103] have studied the displacement of group III,IV,V, & VI elements in Si by 2 MeV He^+ beam. The crystals were damaged by irradiating in a non-aligned direction. The bombardment was interrupted at certain intervals to analyze the introduced displacement effects by channeling along the <110> direction. They found that group IV elements are hardly displaced by the beam particles whereas the displacement rates for other elements are large. They explained the results by assuming a Coulomb attraction between charged point defects and impurity atoms. Negatively charged vacancies in n-type Si are trapped by group V and VI atoms which can be considered as positively charged in the lattice. In p-type Si, the positively charged vacancies are trapped by the negatively charged acceptor atoms. For group IV elements no Coulomb interaction is expected since the impurity atom is uncharged.

From the previous discussion we may conclude;

a) At least for energies in the range 100 keV to 2 MeV $^4He^+$ bombardment of Si produces surface and bulk damage, rather than annealing, both at room temperature and low temperature. (For current densities $\sim 1\mu A/cm^2$).

b) Surface damage exceeds the theoretical prediction.

c) Temperature and incidence direction (i.e. channeled or non-channeled) of $^4He^+$ beam affect the surface rather weakly.

d) Bulk (and surface) damage due to $^4He^+$ beam is not the same for implanted and unimplanted Si.

5-2 Formulation of the problem and method of solution

As far as RBS-channeling is concerned, the important implication is the damage production due to MeV $^4He^+$ and how it depends on the initial state of damage and whether it is simply additive or not.

For this purpose the investigations were carried out at 40 K, with 2 MeV $^4He^+$ beam incident in the <100> direction of undamaged and initially damaged GaAs crystals. The initial damage was introduced by implanting the samples with various doses of 40 keV N^+, 40 keV Bi^+ and 80 keV N_2^+. This makes the comparison of the effect of $^4He^+$ beam under different levels and distributions of damage possible. For purpose of comparison, damage produced was normalized to a saturation damage level which corresponds to complete amorphization.

5-3 Experimental results

a) Determination of damage saturation levels

In order to determine the damage saturation levels; damage vs. implantation flux was plotted for 40 keV N^+ and Bi^+

implantations as shown in fig. (5-1). The values indicated were taken to represent the saturation levels for the nitrogen and bismuth implantations respectively.

b) The unimplanted samples

Fig. (5-2) shows an example of RBS spectra obtained for unimplanted sample. The technique used to collect the spectra is slightly different from that described before. Here, the spectrum obtained due to an analysis (with 2 μC of $^4He^+$) is accumulated over the previous spectrum and so on. This method was found to give more reproducible results[104].

In Fig. (5-3), the number of displaced atoms, N_D, is plotted versus the $^4He^+$ dose. The figure shows the results of three <100> aligned 2 MeV $^4He^+$ bombardment on unimplanted samples. It also shows the results of two experiments in which samples were previously damaged up to about 15% of saturation damage level by 40 keV N^+ bombardment and then subjected to a series of channeling-RBS analyses using 2 MeV $^4He^+$ ions. The reproducibility displayed is quite good even though the statistical errors are about ± 15%. Assuming linear dependence, the best fitting lines were found by least squares method. The average slope is found to be 0.3 for the undamaged sample and 2.4 for the nitrogen implanted sample. The damage cross-section can be found by assuming that the incident beam is composed of two components; aligned and random. The aligned will interact with the scattering centers with 100%

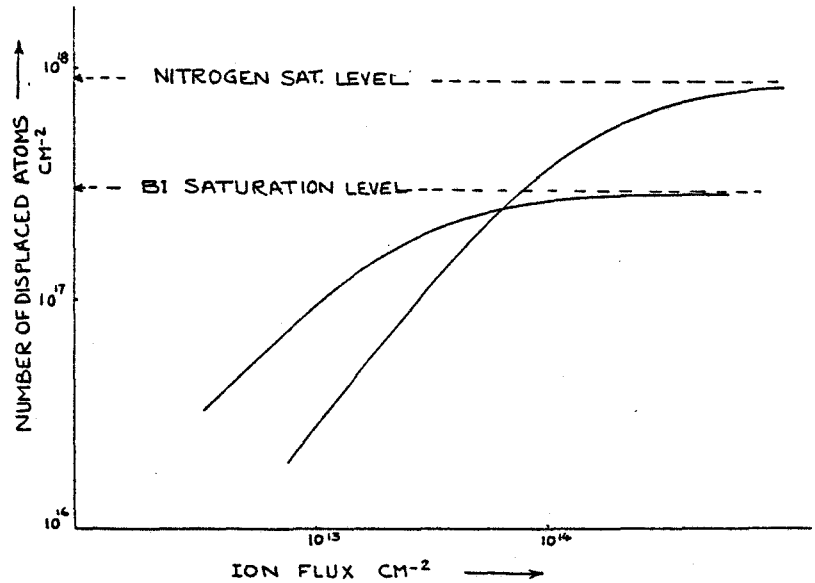

Fig. (5-1) Saturation levels of 40 keV Bi^+ and N^+ implanted into Si.

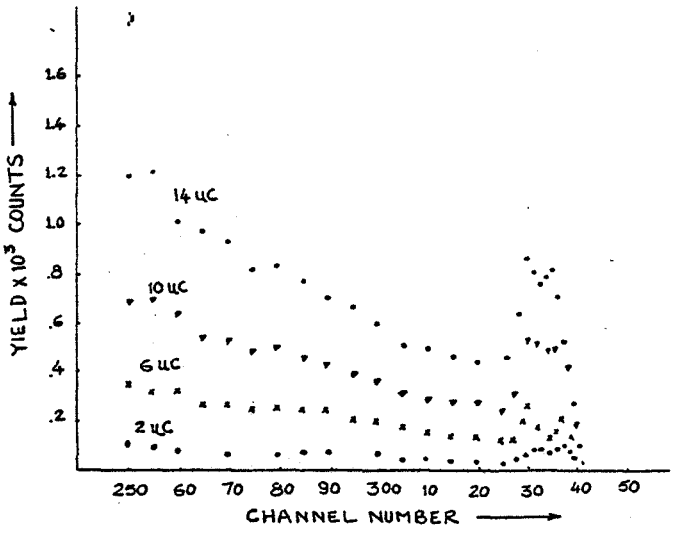

Fig. (5-2) Backscatter spectra of unimplanted GaAs at 40 K.

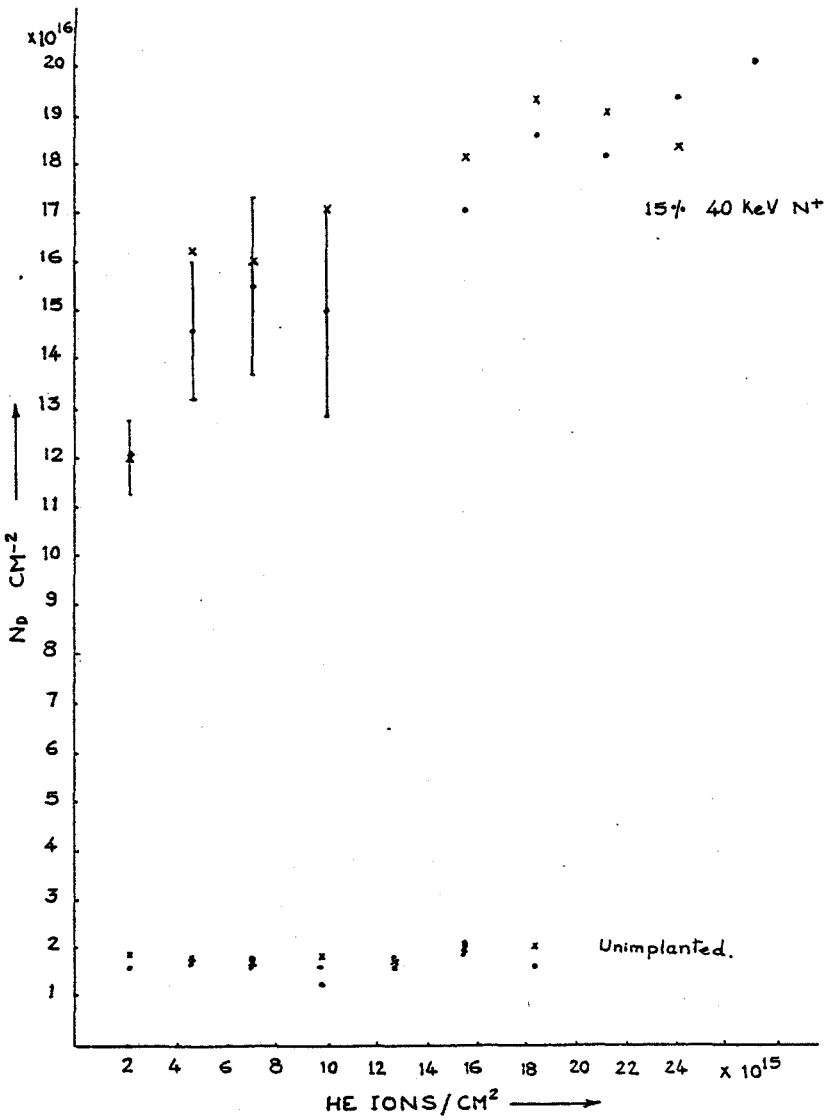

Fig. (5-3) Example of reproducibility of He-beam effect experiments.

probability while the random will interact with all the available atoms with probability σ_D. This leads to;

$$\sigma_D = N_D^*/[(1-\chi_{min})N_{sc}+\chi_{min}NR] \qquad (5-1)$$

where, N_{sc} is the number of scattering centers as determined from the peak of the backscatter spectrum, N is the atomic density and R is the ion range, and N_D^* is the number of displaced atoms per incident ion.

Accordingly, $\sigma_D \simeq 1.8\times10^{-17}$ cm^2 for the unimplanted (χ_{min} = 0 in eq. (5-1)) and $\sigma_D \simeq 2\times10^{-17}$ cm^2 for the nitrogen implanted sample.

c) 40 keV N^+ implanted samples

Fig. (5-4) shows a series of RBS spectra for a sample previously implanted at 40 K with 40 keV N^+ to a dose of 2×10^{13} cm^{-2}. By comparison to fig. (5-2), a faster build up of the damage peak in the implanted sample and a wider peak are observed. The number of displaced atoms is extracted from the spectra and plotted versus the $^4He^+$ ion dose in fig. (5-5). The figure shows the results for GaAs samples initially implanted from about 2% up to about 46% of damage saturation level with 40 keV N^+. Results for initially unimplanted sample are also shown for comparison. Assuming a linear relation, the best fit to the experimental data was determined by the lea st squares method. The slope of the lines is given in table 5-1.

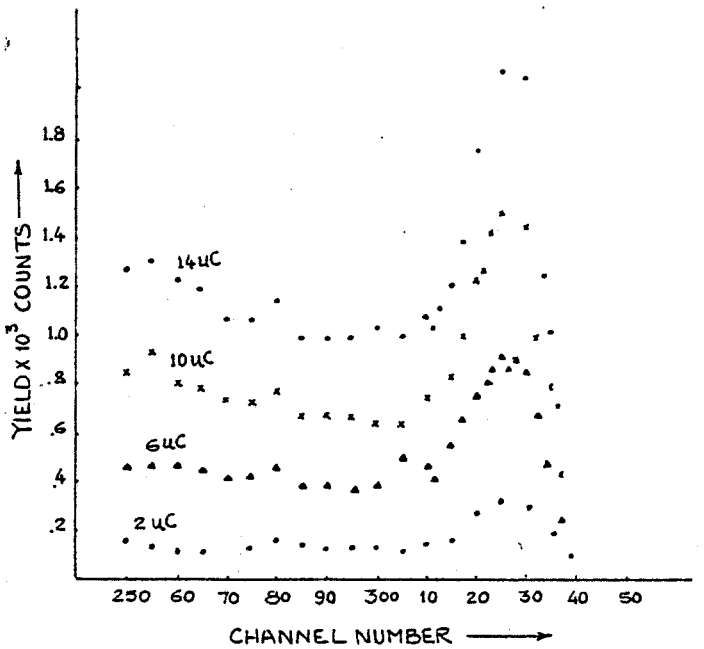

Fig. (5-4) Backscatter spectra of GaAs implanted with 9% of saturation level with 40 keV N^+.

Table (5-1)

$N_D(cm^{-2})$	$1.8x10^{16}$	$7.5x10^{16}$	$1.2x10^{17}$	$3.7x10^{17}$
Approx. damage level %	2	9	15	46
Slope (atoms/ion)	.6	.7	2.4	7
$\frac{1}{N_D} \cdot dN_D/d\phi$	$3.3x10^{-17}$	$9.3x10^{-18}$	$2x10^{-17}$	$1.9x10^{-17}$

d) 80 keV N_2^+ implanted sample

A sample implanted up to about 6% of damage saturation level was subjected to 2 MeV $^4He^+$ bombardment to compare with a sample initially implanted with 40 keV N^+ up to a similar level. Fig. (5-6) shows the results. A comparable slope for the two cases is observed.

e) 40 keV Bi^+ implanted samples

Fig. (5-7) shows the results for samples initially implanted with 40 keV Bi^+ to levels up to about 8%, 28%, and 56% of damage saturation level. Table (5-2) gives the slope of the lines.

Table (5-2)

N_D (cm^{-2})	$2x10^{16}$	$7x10^{16}$	$1.6x10^{17}$
Approx. damage level %	8	28	56
Slope (atoms/ions)	0.5	1	2
$\frac{1}{N_D} \cdot dN_D/d\phi$	$2.5x10^{-17}$	$1.4x10^{-17}$	$1.4x10^{-17}$

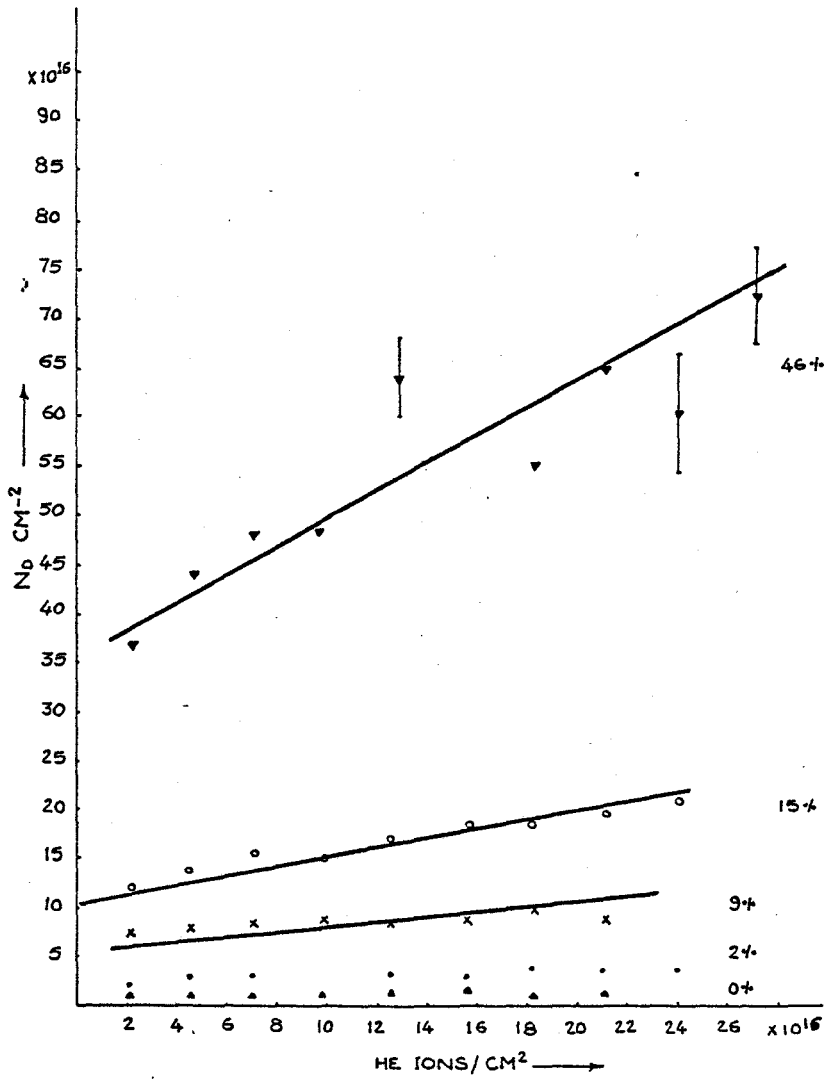

Fig. (5-5) Helium beam damage of <100> GaAs at different levels of initial damage produced by 40 keV N^+ ions.

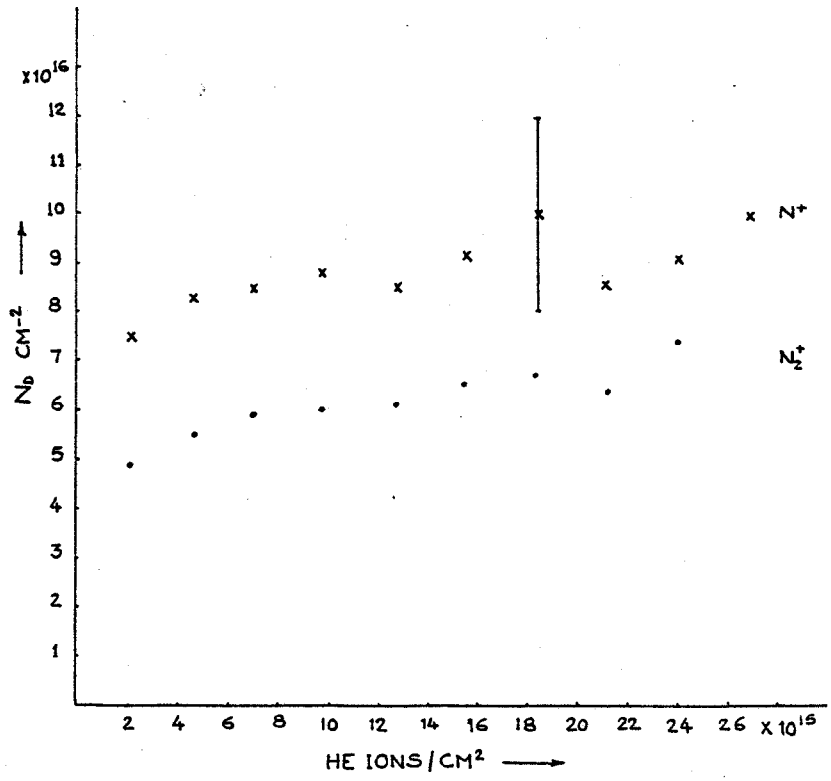

Fig. (5-6) Helium beam damage of <100> GaAs after initial implantation with 40 keV N^+ and 80 keV N_2^+.

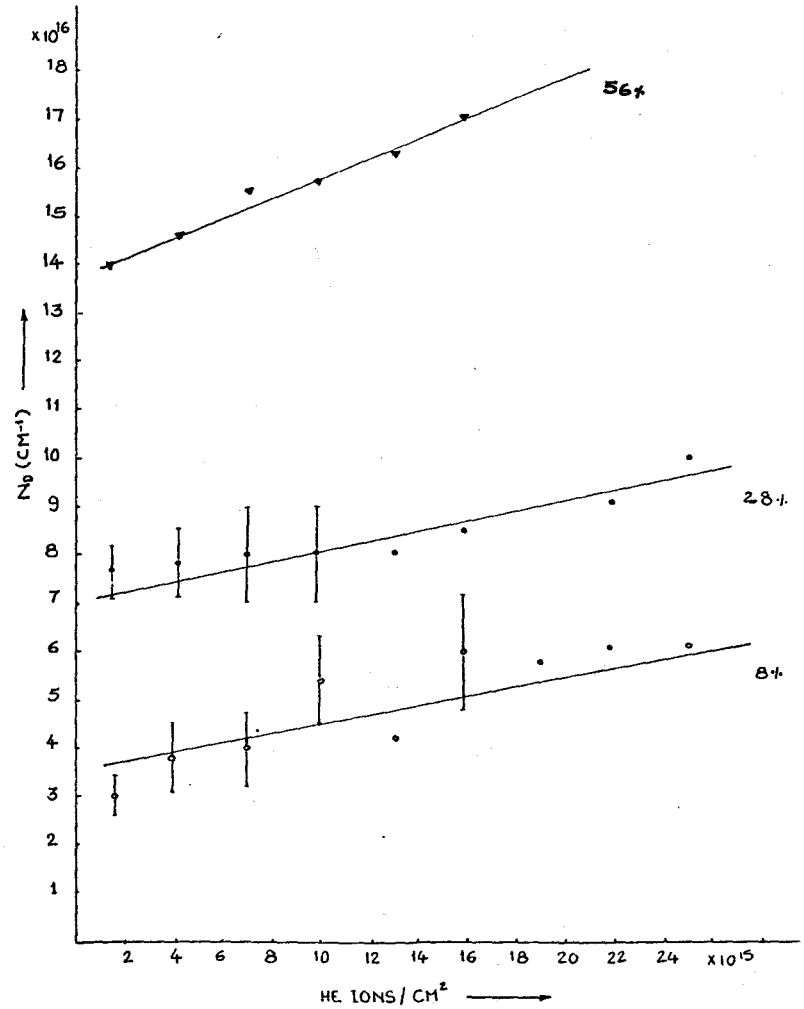

Fig. (5-7) Helium beam damage of <100> GaAs at different levels of initial damage produced by 40 keV Bi^+ ions.

5-4 Discussion

5-4-1 General

Directly from the results presented in section (5-3), it can be concluded that the channeled $^4He^+$ ions produce damage in both unimplanted and implanted samples with the production rate being higher for the implanted ones. This rate is dependent on the initial state of damage. The questions that may arise are;

a) Why the damage production rate increases, in general, with the initial implant dose.

b) How the results compare with theory.

c) How the results compare with the results for Si discussed in the introduction.

5-4-2 Physical Interpretations

From the experimental results presented in the previous section, σ_D was calculated for the unimplanted sample, by assuming that the surface peak in the backscatter spectrum represents the number of scattering centers, and was found to be about 1.8×10^{-17} cm^2. The theoretical prediction for σ_D depends on the way of calculation, varied formulas have been used by different workers.

Kool et al.[101] used for their calculations on Si;

$$\sigma_D = \frac{2\pi a_0^2 M_1 Z_1^2 Z_2^2 E_R^2}{M_2 E_o E_d} \ln \frac{4M_1M_2}{(M_1+M_2)^2} \frac{E_o}{E_d} \qquad (5\text{-}2)$$

where E_R is the Rydberg energy = 13.6 eV.
This equation is based on Kinchin-Pease model[56]. Palmer[73] used a formula that can be reduced to eq. (5-1) multiplied by a factor of 0.8. It is based on the modified Kinchin-Pease model[59], but using the total energy not the elastic energy deposited.

Thompson et al.[10] used for their calculation an equation based on the modified Kinchin-Pease model;

$$\sigma_D = \frac{0.42}{E_d} \int_{E_d}^{T_{max}} \frac{d\sigma}{dT} \cdot T \cdot \nu(T) dT \qquad (5\text{-}3)$$

where, T is the recoil energy and $\nu(T)$ is the fraction of T that is deposited into elastic collision. $\nu(T)$ is approximated by[105];

$$\nu(T) = \frac{1}{K_L g + 1} \qquad (5\text{-}4)$$

where; $K_L = 0.133745\ Z_2^{2/3} / M_2^{1/2}$

$$g = 3.4008\ (\frac{T}{E_L})^{1/6} + 0.40244\ (\frac{T}{E_L})^{3/4} + (\frac{T}{E_L})$$

$$E_L = 86.931\ Z_2^{7/3}\ .$$

This approach is more realistic than the previous ones; the elastic energy deposition by the recoils as a function of their energy is used. Eq. (5-4) is an approximation applicable for the case where $M_1 = M_2$.

Estimating σ_D according to eq. (5-3) gives; $\sigma_D \simeq 3\times10^{-18}$ cm^2 which is less by more than a factor of six than the experimental value given in section (5-2).

To interpret this result, the ideas discussed in chapter III concerning the limitations of the cascade theory may be recalled. For damage produced by MeV light ions, the contribution from spike mechanisms should be minimum, suggesting that the major contribution to damage increase could come from the inelastic part of the deposited energy. In section 3-5 the feasibility of this process in GaAs was discussed from the point of view of times involved. It is also interesting to note that the reported[106,107] upper limits of lifetimes of electrons and holes are large relative to times discussed in section 3-5 (electrons in n-type material, 6×10^{-5} sec., holes 5×10^{-8} sec; electrons in p-type material, 10^{-10} sec, holes 1.5×10^{-4} sec.) The process is also feasible from the point of view of energy. The ionization energy required, E_I, i.e., energy required to create an electron-hole pair can be estimated for GaAs to be about 4.3 eV[108].

The role of the inelastic deposited energy has been investigated by comparing the damage produced by .5 MeV helium beam to that produced by 2 MeV. For this purpose a sample implanted with 40 keV N^+ up to about 46% of damaged saturation level was subjected to .5 MeV He beam bombardment. The value of N_D^*, the number of displaced atoms per incident He^+ ion,

was found to be about 30. This number is about 4 times higher than the number given in table (5-1) for the case of 2 MeV bombardment of a sample initially implanted 40 keV N^+ up to ab out 47% of damage saturation level. Since the increase in $(\frac{dE}{dx})_e$ for .5 MeV over that for 2 MeV He in GaAs is about 10%, while $(\frac{dE}{dx})_n$ is increased by a factor of about 3, it may be inferred that the inelastic energy does not play a major role in damage production, other mechanisms are responsible for the increase in damage production as will be discussed later in this section.

The results of section 5-2 show also that the damage production rate for the implanted samples (up to levels $\sim$ 50% of complete amorphization) is higher than the unimplanted ones. Comparable damage production rate was found for low dose bismuth and nitrogen implanted samples when comparable number of displaced atoms was produced. But at higher doses, higher rates were found for nitrogen implanted samples. This is shown in fig. (5-8). A possible explanation will be discussed here.

As the ions penetrate into the crystal two effects take place; foreign atoms are introduced and damage is produced. Both processes create strain field(s) in the crystal. Since the damage concentration is much higher than the concentration of foreign atoms (e.g. 1 Bi ion produces $\sim 8\times10^4$ displaced atoms), we may neglect the effect of foreign atom strain fields for the present purpose.

A possible consequence of strain field creation is the reduction of the energy required to displace atoms from their

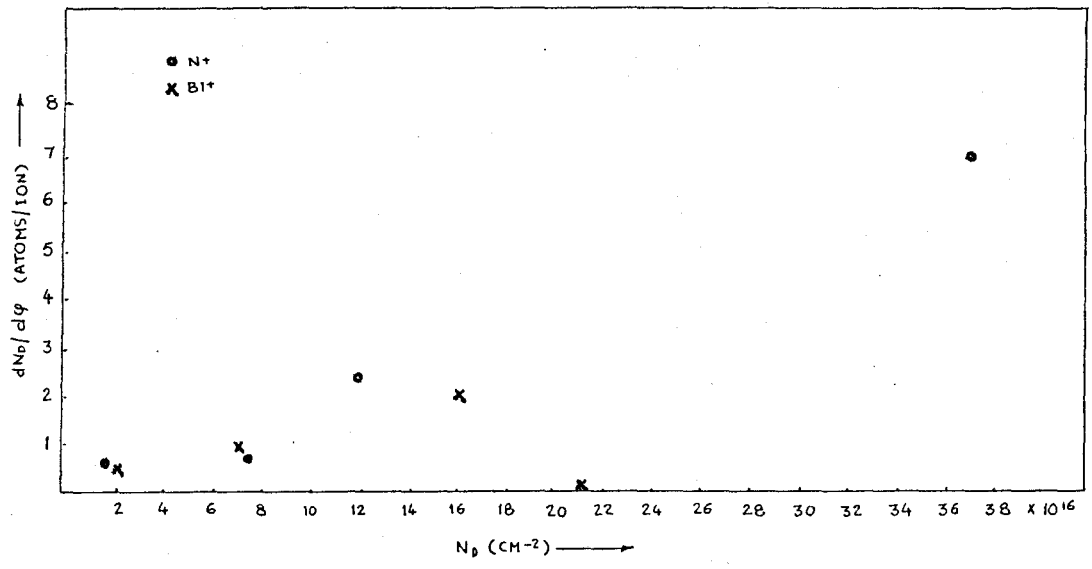

Fig.(5-8) The number of displaced atoms per helium ion vs. the initial number of displaced atoms for 40 keV N^+ and Bi^+ implants into GaAs at 40 K.

lattice sites. As a first approximation we may assume that the strain field(s) is directly proportional to the increase in damage. However, we have also to consider the distribution of the strain field(s) which is certainly related to the damage distribution. Fig. (5-9) shows the cascades of 40 keV N^+ and 40 keV Bi^+ on GaAs as simulated by Monte Carlo method[109] using the code developed by Walker[110]. From this figure we may infer that; for nitrogen implanted samples, there will be a zone of relatively low defect concentration and hence the created strain fields will affect many atoms that are still in lattice sites. While for the Bi-implanted sample, there is a high defect density. The atoms that will be affected, as far as displacing from lattice sites is concerned, are those at the boundaries of the cascade. This can account for the difference in the damage production rates in N- and Bi-implanted samples at relatively higher damage levels.

It is also important to note that Fig. (5-8) shows that the damage production rate $\frac{dN_D}{d\phi}$, increases more rapidly at a damage level of about 15% of saturation, suggesting that automatic collapse to amorphous state may be occuring around that level of damage.

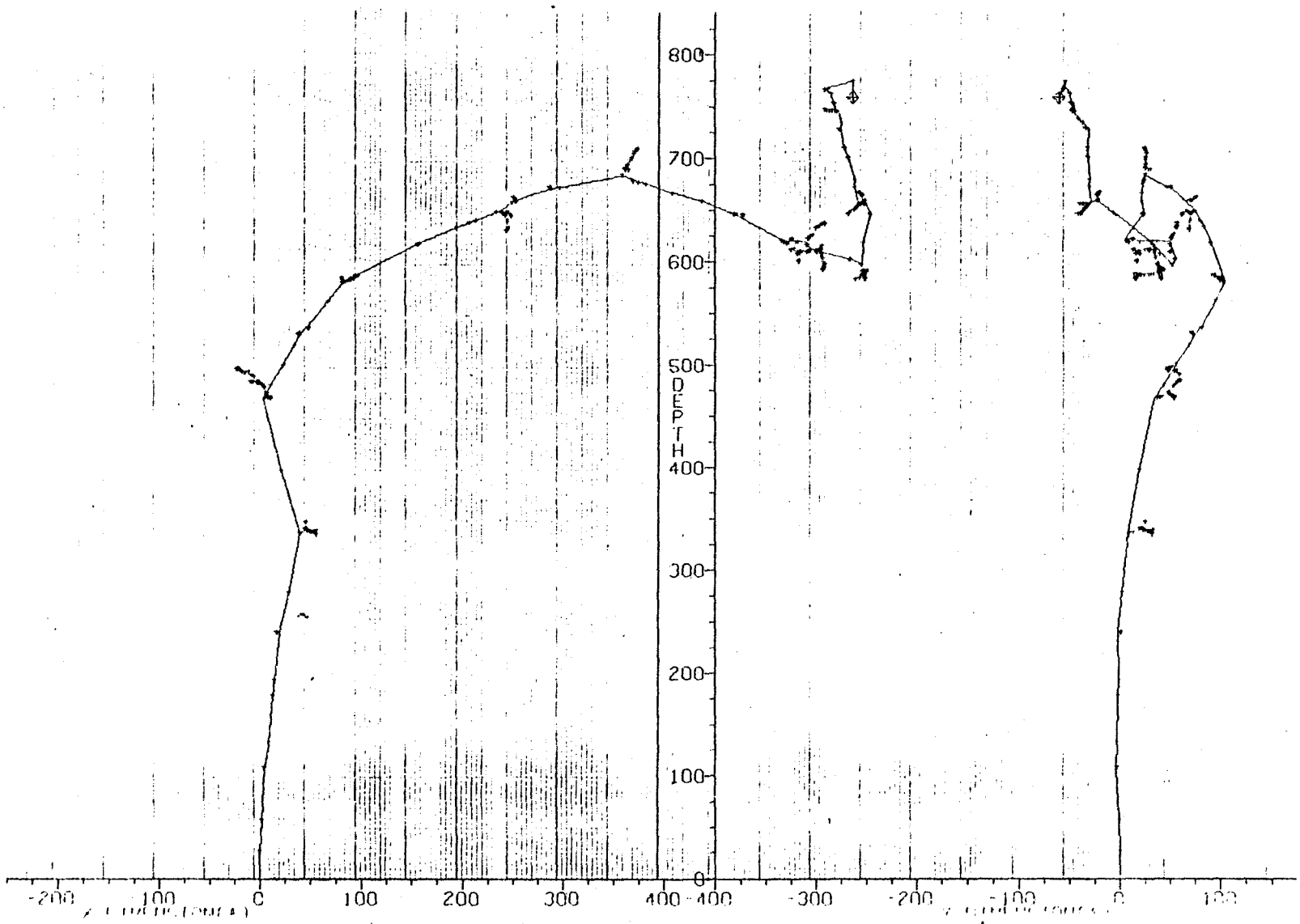

Fig. (5-9) a) Monte Carlo cascades for 40 keV N^+ into GaAs.

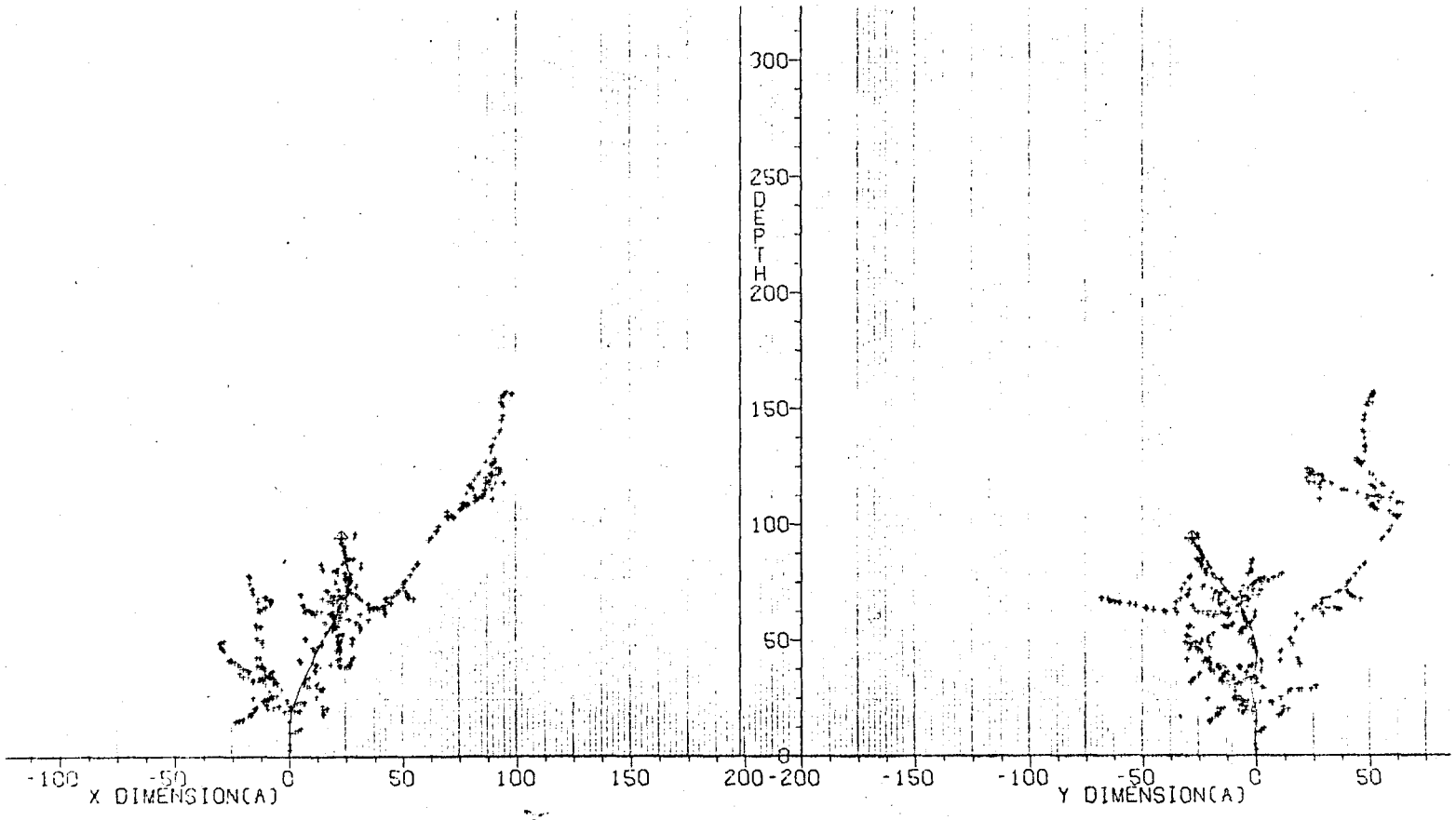

Fig. (5-9) b) Monte Carlo cascades for 40 keV Bi^+ into GaAs.

CHAPTER VI

HEAVY ION IMPLANTATION DAMAGE IN GaAs AT 40 K

6-1 Introduction

In chapter II, it was stated that damage produced in semiconductors by implantation doping plays an important role in the final characteristics of the implanted material. This is the reason for the interest in studying damage production as function of the implanted ion fluence.

Early studies[111,112] in Si at room temperature showed that the disorder increases monotonically with ion fluence until a saturation level is approached. The general behaviour appeared to be independent of ion species, but the saturation level was lower for heavier ion implants. Plotting log (disorder) vs. log (fluence) showed almost unity slope in the presaturation portion. However, subsequent detailed studies[113,114] revealed that in the presaturation region, the $\log(N_D)$ vs. $\log(\phi)$ function had a slope greater than unity for relatively light ion implanted Si at room temperature. Also, it was observed[113,114] that the damage production is dependent on ion flux density. These observations gave rise to the suggestion[115,116] that low mass projectiles produce simple point defects that may migrate, at room temperature, and form clusters. When the local density of point defects reaches a suf-

ficiently high level, catastrophic collapse to an amorphous zone results. Swanson et al.[117] have considered this transformation in Ge. They estimated that; Ge crystal containing defects of .02 - .04 atomic fraction collapses to amorphous state; and they suggest similar results should apply to Si. Lower values may be expected for GaAs since it has weaker bonding. The critical defect concentration computed by Swanson et al. was suggested[118] to be taken as the lower limit at which the crystalline-to-amorphous transition might occur, since the derivation assumes that thermodynamic equilibrium has been achieved. An estimation which is an order of magnitude higher has even been proposed[119]. However, the comprehensive damage-fluence investigations at low temperature by Thompson et al.[120] suggest that the automatic collapse process occurs for defect fractions in the range .02 - .18. This rather supports the predictions of Swanson et al.

On the other hand, the $\log(N_D)$ vs. $\log(\phi)$ plots for heavy ions implanted into Si show unity slope in the presaturation region. This together with no ion flux density dependence and TEM studies[121] suggests that heavy ions create direct impact amorphization of small zones.

Baranova et al.[122] and Sobolev et al.[123] have argued that both simple defect formation and direct impact amorphisation can occur under all impact conditions, the relative magnitude of each depends on the energy deposition density in the cascades and the subcascades produced by each projectile.

In order to investigate the effect of varying the energy density associated with a single cascade without varying any of the implant parameters, one can use diatomic ions having the same energy per atom as the corresponding monatomic ions. As the diatomic molecule hits the target surface, it dissociates into two ions, each producing damage cascade. The degree of overlapping of the two cascades determines the enhancement in the energy density. For complete overlap, the energy density will be doubled. The energy spike becomes more significant as the energy density increases. Such investigations have been carried out[124,125] in Si and Ge both at 300 K and 50 K for various ions in the energy range 10 - 60 keV per atom. These investigations have shown that the enhancement in damage due to diatomic implants, as expressed by N_D^* (mol.)/2 . N_D^* (atom), increases monotonically with the projectile mass and decreases with the increase of projectile energy. These findings will be discussed in more detail in section (6-3).

Similar investigations have been carried out[65] in GaAs at room temperature for arsenic ions having 20 keV per atom. The damage due to diatomic implants was found to be two to three times larger than that due to monatomic implants.

This chapter reports on a systematic investigation of damage-fluence behavior for 40 keV N^+, Sb^+, As^+ and Bi^+ ions. Comparison with the corresponding diatomic implants at 80 keV is also reported. The investigation has been carried out at 40 K to minimize the annealing effects.

6-2 Experimental results

Figures (6-1) to (6-4) show the variation in the measured total number of displaced atoms, N_D, as a function of the implantation dose ϕ, for 40 keV monatomic and 80 keV diatomic implantations with nitrogen, arsenic, antimony, and bismuth into GaAs. In all the figures N_D is plotted vs. ϕ on: a) linear-linear and b) log-log graphs. The linear-linear graph facilitates the comparison between the molecular and atomic implants while the log-log graph shows the overall behaviour of N_D vs. ϕ.

The main features of these graphs are:

a) The monatomic and diatomic implants with the same species have the same saturation level. This is important to note because it ensures that the implants are the molecular and atomic ions of the same ion species with the same energy per atom.

b) The saturation levels decrease with increasing ion mass as expected from range consideration.

c) The presaturation portions show linear behaviours within the experimental error.

d) The ratio N_D^* (mol)/2 N_D^* (atom) is almost unity for all the implants.

Table (6-1) summarizes the main features of the graphs and gives a comparison between the experimental number of dis-

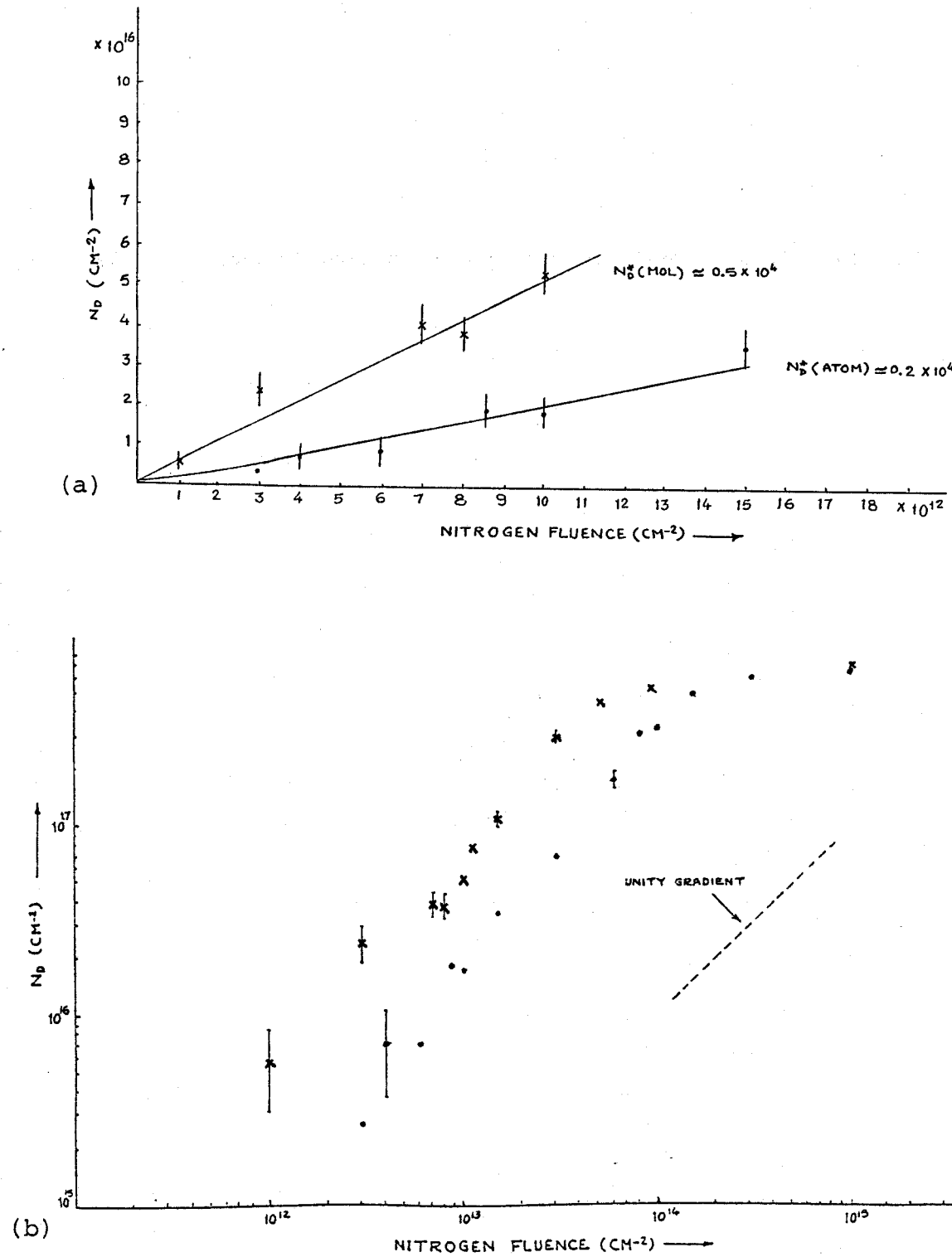

Fig. (6-1) Atomic and molecular nitrogen damage in GaAs for 40 keV per atom implants at 40 K.

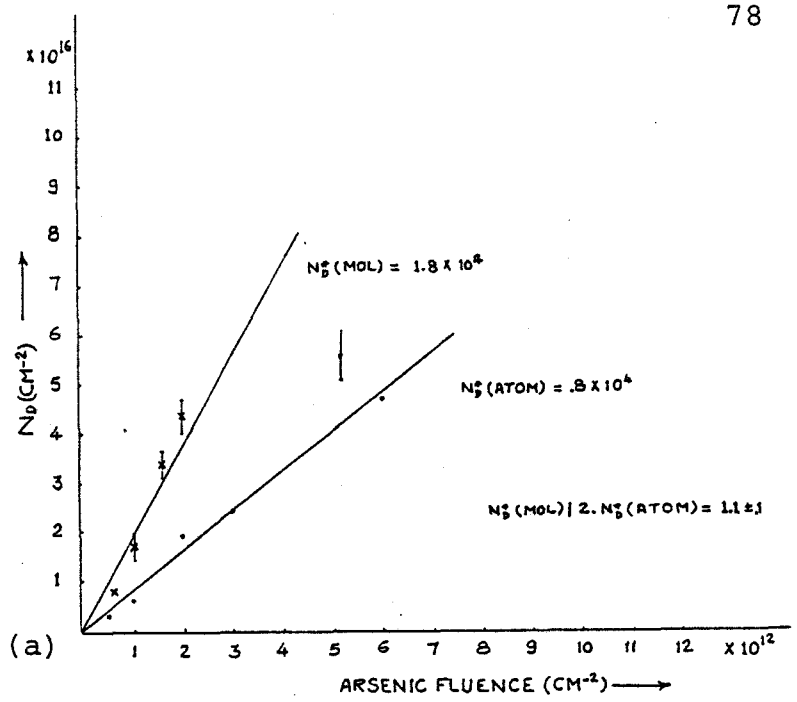

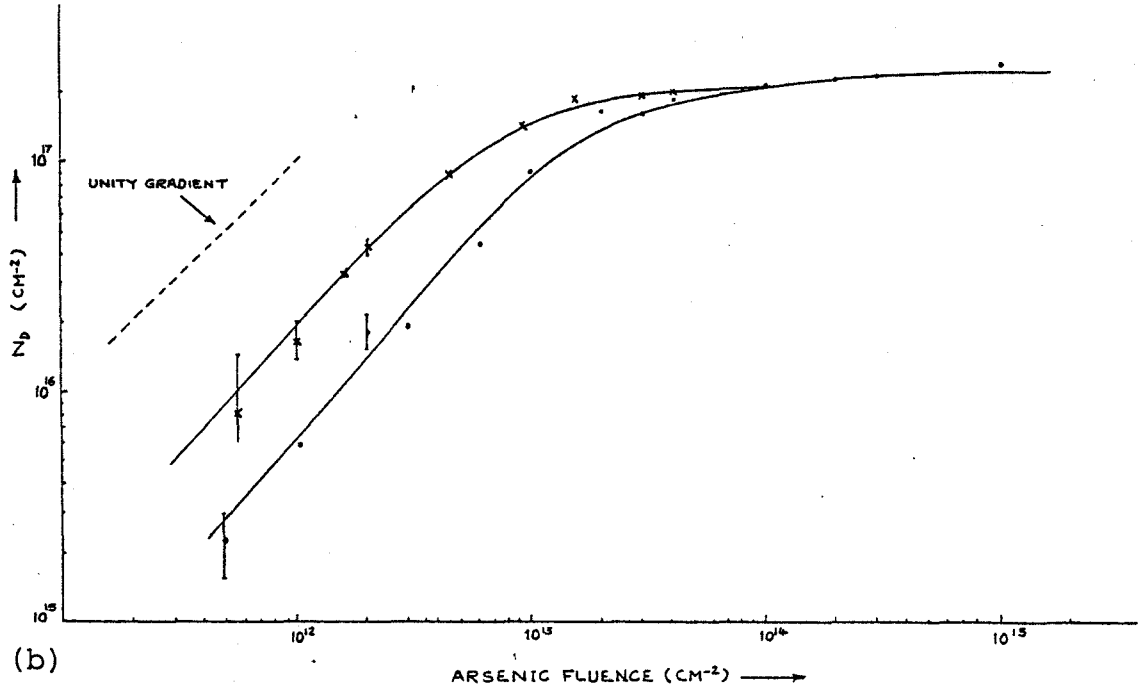

Fig. (6-2) Atomic and molecular arsenic damage in GaAs for 40 keV per atom implants at 40 K.

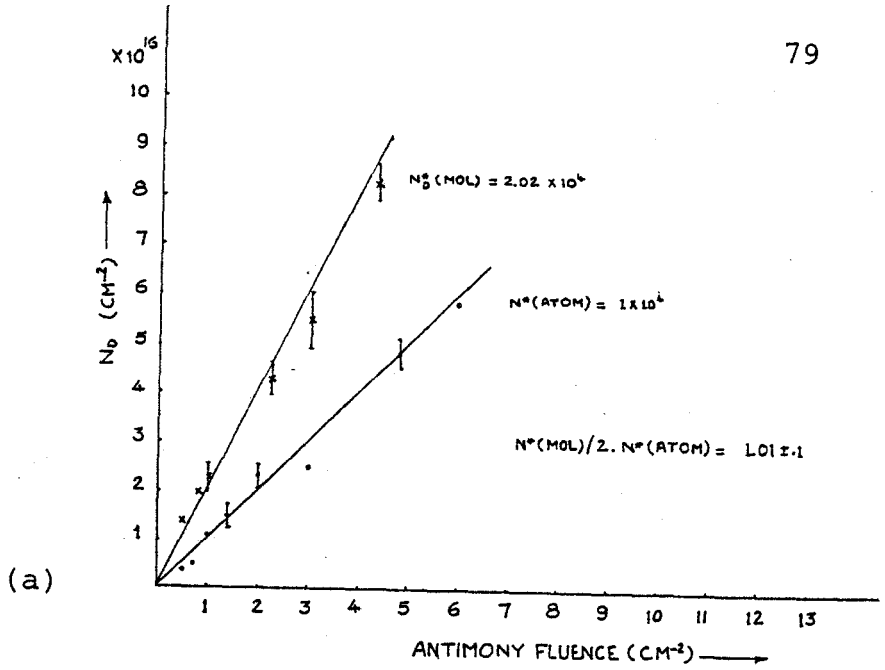

(a)

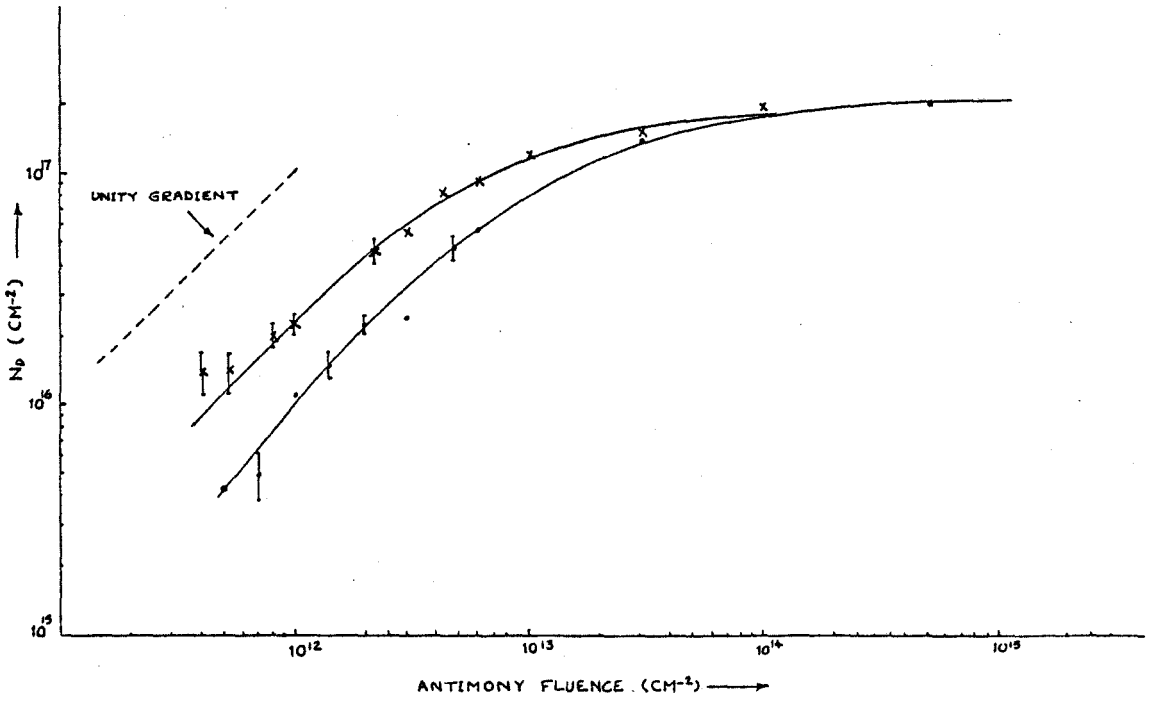

(b)

Fig. (6-3) Atomic and molecular antimony damage in GaAs for 40 keV per atom implants at 40 K.

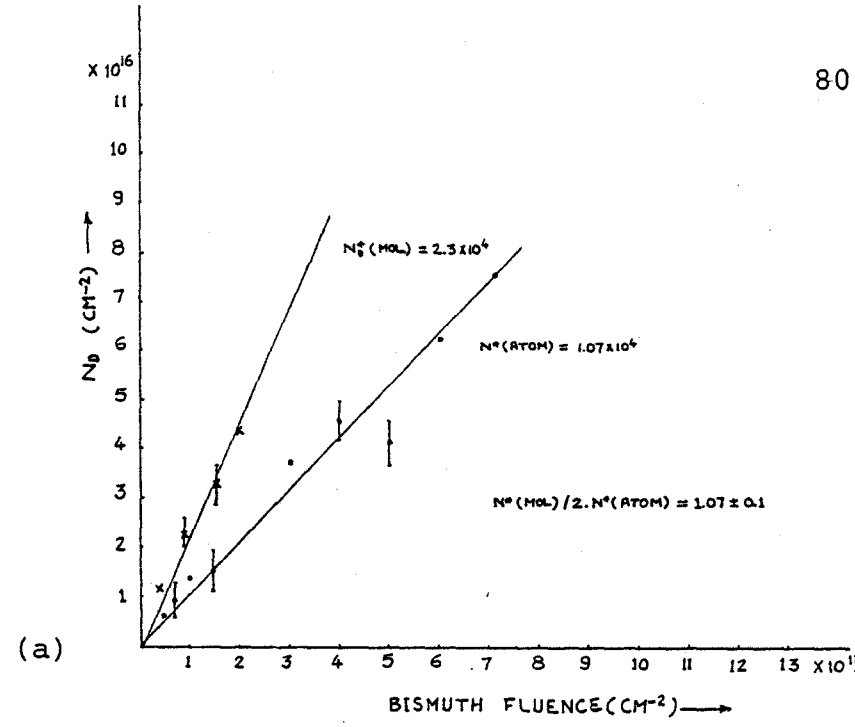

(a)

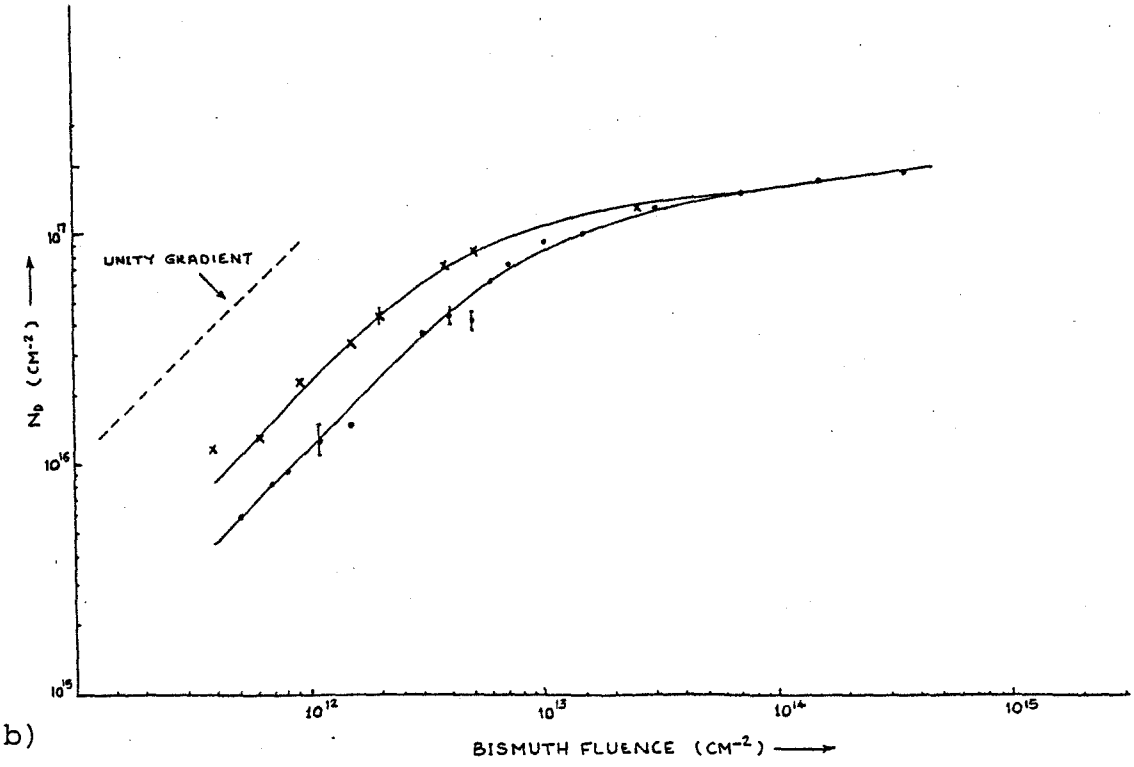

(b)

Fig. (6-4) Atomic and molecular bismuth damage in GaAs for 40 keV per atom implants at 40 K.

placed atoms per ion, N_D^*, and the value predicted by Kinchin-Pease equation, N_{K-P}. It can be seen that the experimental values are higher than the theoretical predictions. Moreover, the higher the mass of the incident ion, the higher the deviation from the theoretical predictions.

Table (6-1)

Ion	Energy	$N_{sat.}$ ($\times 10^{-17}$ cm^{-2})	N_D^*(atom) $\times 10^{-4}$	$\frac{N_D^*(mol.)}{2N_D(atom)}$	N_{K-P}^*	N_D^*/N_{K-P}
N	40	7.3	.23	1.08±.1	819	2.8
N_2	80	7.3	.5			
As	40	2.8	.8	1.1 ±.1	1272	6.2
As_2	80	2.8	1.8			
Sb	40	2	1	1.01±.1	1319	7.5
Sb_2	80	2	2.02			
Bi	40	1.8	1.07	1.07±.1	1357	7.8
Bi_2	80	1.8	2.3			

Since the purpose of diatomic implants was to change the energy density within the cascade, it is important to calculate the energy density, $\bar{\theta}_\nu$ ev/atom. This can be calculated as follows[109];

a) for monatomic implants, $\bar{\theta}_\nu = 0.2\ \nu(E) E_{atom}/N.V_{casc}\ R_v$

b) for diatomic implants, $\bar{\theta}_\nu = 0.2\ \nu(E) E_{mol}/N.V._{casc} R_v(2-R_v)$

where E_{atom} = energy of monatomic implants = $\frac{1}{2} E_{mol}$,

N = atomic density

V_{casc} = is the average cascade volume calculated from the second order moments, i.e. $V_{casc} = \frac{4}{3}\pi <\Delta x^2>^{1/2} <y^2>$, where $<\Delta x^2>^{1/2}$ corresponds to the longitudinal deposited energy straggling, and $<y^2>^{1/2}$ is the corresponding transverse straggling and $<x>$ is the mean depth of energy deposition,

and R_v defines the fraction of the statistical cascade volume fitted on average by an individual cascade as determined from Monte Carlo calculations. For 50 cascades the statistical uncertainty in R_v is $\sim$ 10 - 20%.

Table (6-2) gives the above parameters as calculated for GaAs[127]. For dilute cascades, e.g. for 40 keV N^+, the calculated $\bar{\theta}_\nu$ in table (5-2) is overestimated. For denser cascades, it becomes more reliable.

6-3 Discussion

To describe the damage-fluence function analytically[127], it is assumed that each projectile displaces $N_D^*(x)dx$ lattice atoms in a depth interval dx. The increase in the total number of displaced atoms, $dN_D(x)dx$, due to incremental increase in $d\phi$ in the fluence of the projectile will be;

Table (6-2)

Ion	Energy (keV)	$\nu \cdot E$ (keV)	$\langle x \rangle$ (Å)	$\langle \Delta x^2 \rangle^{1/2}$ (Å)	$\langle y^2 \rangle^{1/2}$ (Å)	V_{casc} ($A^{\circ 3}$)	R_v	$\bar{\theta}_\nu$ (ev/atom)
N	40	17.94	535.2	352	303.7	1.36×10^{8}	0.00128	0.47
N_2	80	35.90					0.00256	0.47
As	40	27.87	140.4	85.8	58.8	1.24×10^{6}	0.202	0.5
As_2	80	55.70					0.363	0.56
Sb	40	28.91	109.4	66.2	43.9	5.34×10^{5}	0.397	0.62
Sb_2	80	57.8					0.636	0.77
Bi	40	29.73	89.51	53.3	34.5	2.66×10^{5}	0.546	0.93
Bi_2	80	59.50					0.794	1.28

$$dN_D(x)dx = N^*_D(x)dx[1 - \frac{N_D(x)}{N_{sat.}}]d\phi \qquad (6\text{-}1)$$

$N_{sat.}$ represents the number of displaced atoms at saturation and hence $[1-N_D(x)/N_{sat.}]$ represents the number of atoms available for displacement.

Solution of eq. (6-1), for small values of ϕ, gives;

$$N_D = N^*_D \phi \qquad (6\text{-}2)$$

Eq. (6-2) predicts that the presaturation portion of $\log(N_D)$-$\log(\phi)$ curve is linear and has unity slope. This is consistent with the results of section (6-1) that shows unity slope behavior for heavier ions (As^+, Sb^+ and Bi^+) and low of implant doses ($\sim$ 10% of saturation) for N^+. If there were disorder zone overlap the log N_D/log ϕ plot would exhibit superlinearity[127,128].

From table (6-1), it can be seen that the measured N^*_D exceeds the theoretical predictions as reported previously for Si[120]. The enhancement of the damage may be attributed to the formation of small damage clusters with amorphous structure. The local transformation to amorphousness may be due to an energy spike. The spike may initiate the process by at least two mechanisms[110];

a) Local heating of the lattice that is associated with the energy spike can destroy the long-range order within the heated region.

b) Accompanying the thermal activation of the lattice atoms due to the energy spike is an increased lattice instability. The unstable lattice may then collapse athermally into amorphous structure.

Assuming[110] that the measured damage is comprised of two components; N_{kp}, due to the collision cascade and N_s due to the energy spike, N_D^* becomes;

$$N_D^* = N_{kp} + N_s. \qquad (6-3)$$

This concept has led to the derivation of semi-empirical formulas for N_D^*;

$$N_D^* = 251 M_1^{3/4} [1-\exp(-\frac{\nu \cdot E}{30(keV)})] + 0.032\ \nu \cdot E \text{ in Si} \qquad (6-4)$$

and

$$N_D^* = 9.1\times10^3 M_1^{1/2} [1-\exp(-\frac{\nu \cdot E}{270(keV)})] + 0.032\ \nu \cdot E \text{ in Ge} \qquad (6-5)$$

Eq. (6-5) seems to be applicable for GaAs as shown in fig. (6-5).

However, two points should be noted;

a) The assumption that N_D^* is comprised of two independent components; N_{kp} and N_s, is not physically justified since N_s is dependent on N_{kp}.

b) The athermal collapse of the lattice occurs when the defect density reaches its critical value and this does not have to come after the thermal spike. It can be reached by overlapping of cascades[129].

In section (6-2), it was reported that; the damage enhancement factor, $N_D^*(mol)/2N_D^*(atom)$, is unity within the experimental errors. In other words, there is no observable en-

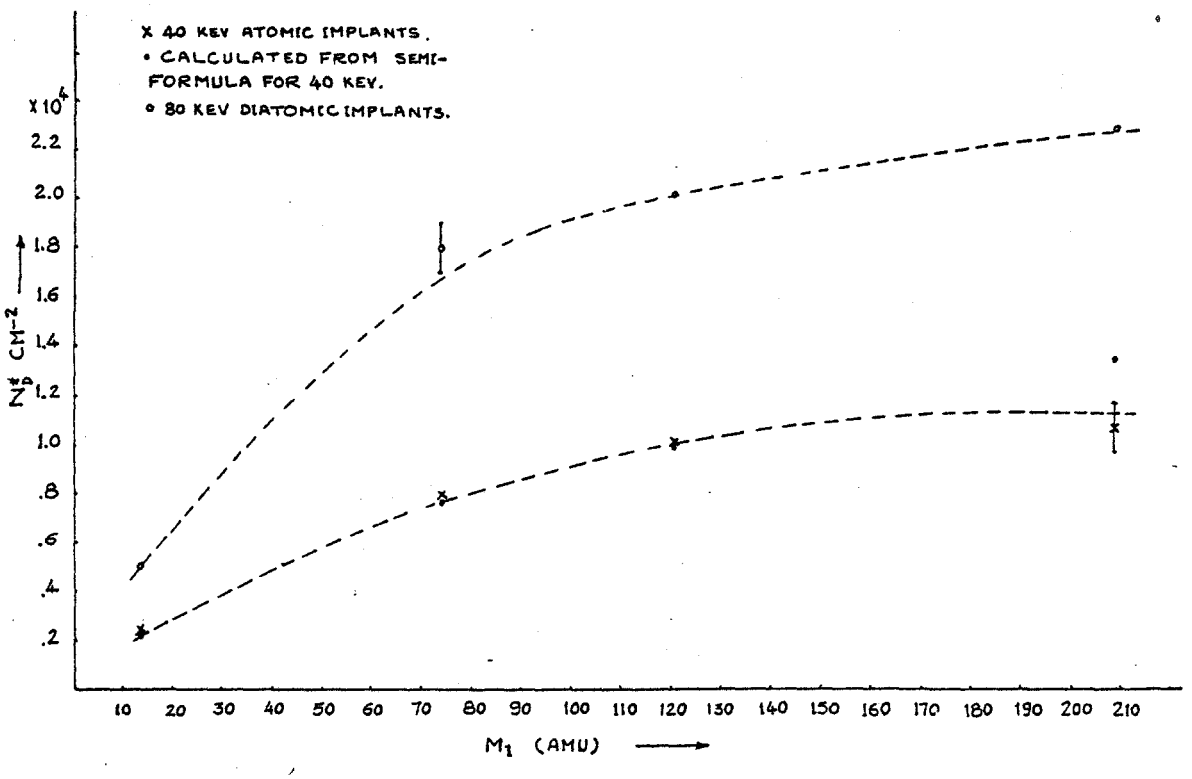

Fig. (6-5) Damage vs. incident ion mass.

hancement in damage production due to diatomic implantations. This does not contradict the results reported by Moore et al.[125] for atomic and molecular implants into GaAs because it was carried out at different experimental conditions;

a) room temperature implantation

b) lower energy, i.e., 20 keV/atom not 40 keV/atom.

At room temperature, it is expected that the damage enhancement will be greater than at 40 K because in the former case two competing processes exist, namely, energy spike and annealing effects. The enhancement at room temperature has been observed also in Si and Ge. The factor $N_D^*(300K)/N_D^*(35K)$ is reported to increase towards unity as $\bar{\theta}_\nu$ increases.

The enhancement factor, $N_D^*(mol)/2N_D^*(atomic)$, is a function of the implant ion energy. As the ion energy increases, the energy-spike becomes of decreasing significance and hence the enhancement factor approaches unity. This energy dependence has been reported for Si[110], fig. (6-6) shows $[N_D^*(mol)/2N_D^*(atomic)]$ as function of ion energy for arsenic implants. This figure shows that at energies of about 40 keV per atom and higher, the enhancement factor approaches unity within the experimental error.

The third parameter that affects the enhancement factor is the ion mass. For light ion masses, discrete and isolated subcascades develop within the cascade envelope. Hence the probability of overlap of the branches of cascades of individual atoms of the molecular ions is lower for light ions, i.e.

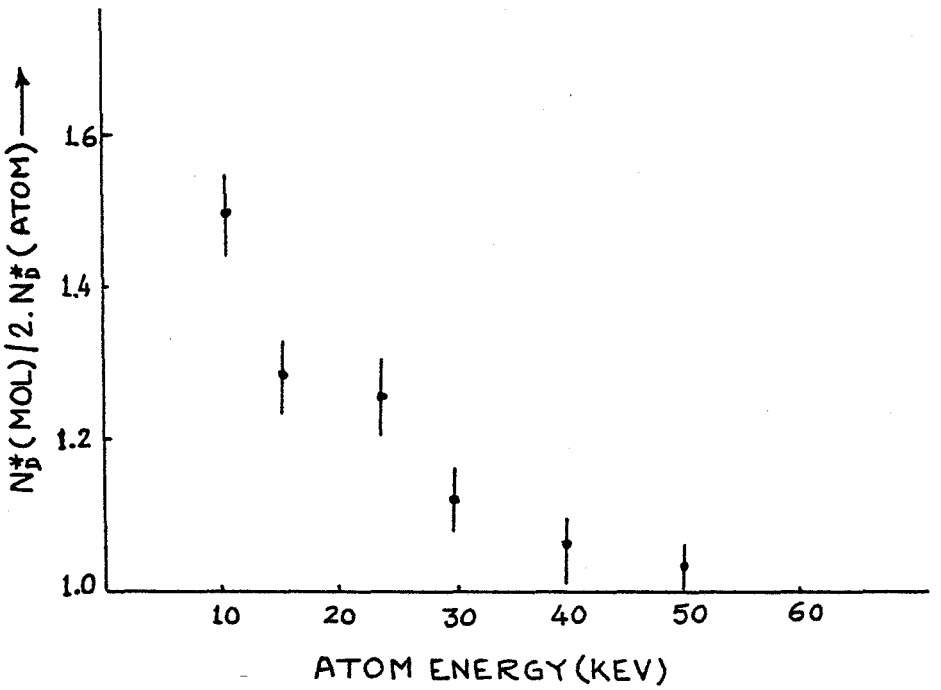

Fig. (6-6) The ratio $N_D^*(mol)/2.N_D^*(atom)$ versus ion energy per atom for arsenic implants into Si at 33 K. (Ref. 110)

the local energy density associated with these cascades will not be increased significantly.

CHAPTER VII

SUMMARY

The conclusions that have been drawn from the work discussed in the previous chapters may be summarized as follows:

1. Damage production exceeds, in general, the theoretical prediction by factors of 3-8.

2. The rate of damage production by 2 MeV He ions is dependent on the state of initial state of damage and increases, in general, with the increase of the initial damage.

3. The inelastic deposited energy has no major contribution in damage production.

4. Heavier ions (40 keV As^+, Sb^+ and Bi^+), may produce amorphous zones directly within the individual collision cascades.

5. No enhancement in damage production due to molecular implants was noticed in consitence with the results for Si at the same energy used.

REFERENCES

1. W.K. Hofker and J. Politiek, Phil. Tech. Rev. 39, 1 (1980).
2. M.W. Thompson, Defects and Radiation Damage in Metals, Cambridge Univ. Press (1969).
3. J.P. Donnelly, Nucl. Instr. and Methods 182/183, 553 (1981).
4. G. Foti, Nucl. Instr. and Methods 182/183, 573 (1981).
5. R.S. Ohl, Bell Sys. Tech. 31, 104 (1952).
6. F.W. Eisen, Rad. Effects 47, 99 (1980).
7. W.H. Weisenberger, S.T. Picraux, F.L. Vook, Rad. Effects 9, 121 (1971).
8. N.A.G. Ahmed, C.E. Christodoulides, and G. Carter, Rad. Effects 52, 211 (1980).
9. J. Mayer, L. Erikson and J. Davies, Ion Implantation in Semiconductors, Academic Press (1970).
10. D.A. Thompson, G. Carter, H.K. Haugen and D.V. Stevanovic, Rad. Effects 46, 71 (1980).
11. D.M. Taylor, D.O. Wilson and D.H. Phillips, IEEE Proc. 127, 266 (1980).
12. A.R. Molozzi, Can. Elec. Eng. 8, 24 (1981).
13. J.B. Gunn, Solid St. Comm. 1, 88 (1963).
    ———, IBM J. of Res. Develop. 8, 141 (1964).
14. W.N. Carr, IEEE Trans. Electron Dev. ED-12, 531 (1965).

15. N. Bar-Chaim, I. Ury and A. Yariv, IEEE Spectrum, 19 No.5, 38 (1982).

16. J.M. Woodall and H.J. Hovel, J. Vac. Sci. Technol. 12, 1000 (1975).

17. H.M. Hobgood, Graeme W. Eldridge, Donvan L. Barrett, and Noel Thomas, IEEE Trans. Electronic Dev. ED-28, 140 (1981).

18. Robert D. Fairman, R.T. Chen, John Oliver and Daniel R. Ch'en, IEEE Trans. Electronic Dev. ED-28, 135 (1981).

19. O. Madelung, Phys. of III-V Compounds, John Wiley (1964).

20. R.Z. Bacharch, Prog. Crystal Charct. Vol. 2, (1979). p 115

21. C. Hilusum and A.C. Rose-Innes, Semiconducting III-V Compounds, Pergamon Press (1961).

22. C. Kittel, Introduction to Solid State Physics, John Wiley (1976).

23. R. Bauerlein, Radiation Damage in Solids. Proc. International School of Physics, Academic Press, New York, p. 358 (1962).

24. E.E. Klontz and K. Lark-Horvitz, Phys. Rev. 82, 763 (1951).

25. J.J. Loferski and P. Rappaport, Phys. Rev. 98, 1861 (1955). Phys. Rev. 111, 432 (1958).

26. G. Carter and J.S. Colligon, Ion Bombardment of Solids, American Elsevier Publishing Company (1968).

27. W.L. Brown and W.M. Augustyniak, J. Appl. Phys. 30, 1300 (1959).

28. J.A. Grimshaw and P.C. Banbury, Proc. Phys. Soc. (London) 84, 151 (1964).

29. S.M. Sze, Physics of Semiconductor Devices, John Wiley (1969).

30. J. Lindhard and M. Scharff, Phys. Rev. 124, 128 (1961).

31. See for example, H. Goldstein, Classical Mechanics, Addison-Wesley, Cambridge, Mass. (1958).

32. N. Bohr, Mat. Fys. Medd Dan Vid Slesk, 18, No. 8 (1948).

33. E. Rutherford, Phil. Mag. 21, 669 (1911).

34. J. Lindhard, M. Scharff and H.E. Schiøtt, Mat. Fys. Medd Dan Vid Slesk, 33, No. 14 (1962).

35. D.K. Holmes, Radiation Damage in Solids Vol. 1, International Atomic Energy Agency Vienna (1962).

36. M. Born and J.E. Mayer, Z. Physik 75 (1), 96 (1932).

37. O.S. Oen, D.K. Holmes and M.T. Robinson, J. Appl. Phys. 34, 302 (1963).

38. G. Moliére. Z. Naturforsch 2a, 133 (1947).

39. A.A. Abrahamson, R.D. Hatcher and G.H. Vineyard, Phys. Rev. 121, 159 (1961).

40. A.A. Abrahamson, Phys. Rev. 130, 693 (1963).

41. A.A. Abrahamson, Phys. Rev. 133A, 990 (1964).

42. J. Lindhard, Mat. Fys. Medd Dan Vid Slesk 34, No. 14 (1965).

43. O.B. Firsov, Sov. Phys. JETP 6 (33), 534 (1958).

44. P. Gombas, Handbuch der Physik, Ed. XXXVI (1956).

45. J. Lindhard, V. Nielsen and M. Scharff, Mat. Fys. Medd. Dan Vid Slesk. 36, No. 10 (1968).

46. J. Lindhard, V. Nielsen, N. Scharff and P.V. Thomson, Mat. Fys. Medd. Dan. Vid Slesk. 33, No. 10 (1963).

47. H.A. Bethe, Ann. Phys. 5, 325 (1930).

48. J. Lindhard and A. Winther, Mat Fys. Medd Dan Vid Slesk 34, 4 (1964).

49. O.B. Firsov, Zh. Eksp Teor. Fiz. 36, 1517 (1959).

50. F.H. Eisen, Can. J. Phys. 46, 561 (1968).

51. J. Bøttiger and F. Bason, Rad Effects. 2, 105 (1969).

52. I.M. Cheshire, G. Dearnaley and J.M. Poate, Phys. Lett. 27A, 304 (1968).

53. C.P. Bhalla, J.N. Bradford and G. Reese, Atomic Collision Phenomena in Solids (Eds. Townsend, Palmer and Thompson), North-Holland, 361 (1970).

54. J.S. Briggs, A.P. Pathak, J. Phys. C, Solid State Physics, 6, L153 (1973).

55. W.H. Bragg and R. Kleeman, Phil. Mag. 10, 5318 (1905).

56. G.H. Kinchin and R.S. Pease, Rep. Prog. Phys. 18 (1), 143 (1955).

57. M.T. Robinson, Phil. Mag. 12, 741 (1965).

58. M.T. Robinson, Phil. Mag. 17, 639 (1968).

59. P. Sigmund, Appl. Phys. Letts. 14, no. 3, 114 (1969).

60. K.B. Winterbon, P. Sigmund and J.B. Sanders, Mat. Fys. Medd. Kgl. Dan. Vid. Slesk. 37, no. 14 (1970).

61. H. Cramer, Mathematical Methods of Statistics, Princeton Univ. Press, Princeton, N.J. (1946).

62. E.M. Baroody, J. Appl. Phys. 36, 3562 (1965).

63. R.S. Nelson, The Observation of Atomic Collisions in Solids, North Holland Publ. Co., Amsterdam (1968).

64. H.H. Andersen and H.L. Bay, J. Appl. Phys., 46, 2416 (1975).

65. J.A. Moore, G. Carter and A.W. Tinsley, Rad. Effects 25, 49 (1975).

66. J.B. Mitchell,J.A. Davies, L.M. Howe, R.S. Walker and K.B.Winterbon, Ion Implantation in Semiconductors, ed. S. Namba, p. 493 (1975).

67. D.A. Thompson and R.S. Walker, Nucl. Instr. and Methods. 132, 281 (1976).

68. D.A. Thompson and R.S. Walker, Rad. Effects 30, 37 (1976).

69. D. A. Thompson and R.S. Walker, Rad. Effects, 31, 1 (1977).

70. G. Foti, G. Vitali and J.A. Davies, Rad. Effects, 32, 187 (1977).

71. G. Dearnaley, Appl. Phys. Letts. 26, 499 (1975).

72. J.C. Bourgoin, Radiation Damage Processes in Materials, ed. C.H.S. Dupuy (Leyden: Noordhof) p. 339 (1975).

73. D.W. Palmer, Radiation Damage and Defects in Semiconductors, Inst. Phys. Conf. Ser. 31, p. 144 (1977).

74. J.A. Brinkman, J. Appl. Phys. 25, 961 (1954).

75. J.A. Brinkman, Am. J. Phys. 24, 246 (1956).

76. D.A. Thompson, Rad. Effects, 56, 105 (1981).

77. F. Seitz and J.S. Koehler, Progress in Solid State Physics, 2, 305 (1956).

78. M.W. Thompson and R.S. Nelson, Phil. Mag. 7, 2015 (1962).

79. R. Kelly, Rad. Effects, 32, 91 (1977).

80. R. Kelly, Surf. Science, 90, 280 (1979).

81. C.R. Elliott, T. Ambridge and R. Heckingbottom, Sol. St. Elec., 21, 859 (1978).

82. E. Bøgh, Can. J. Phys. 46, 653 (1968).

83. R.L. Hines, J. Appl. Phys. 28, 587 (1957).

84. J.H. Crawford and L.M. Slifkin, Point Defects in Solids, Vol. 2 (Ch. 4), Plenum Press, New York-London (1972).

85. J.R. Parsons, Phil. Mag. 12, 1159 (1965).

86. E. Rutherford, Phil. Mag. 21, 669 (1911).

87. C.G. Darwin, Phil. Mag. 28, 499 (1914).

88. Wei-kan Chu, J.W. Mayer and Marc-A. Nicolet, Back-scattering Spectroscopy, Academic Press (1978).

89. See for example; W.D. Mackintosh and J.A. Davies, Anal. Chem. 41, 26A (1969).

90. L.C. Feldman and J.W. Rodgers, J. Appl. Phys. 41, 3776 (1970).

91. S.U. Campisano, G. Foti, F. Grasso and E. Rimini, Atomic Collisions in Solids, Vol. 2, Ed. S. Datz et al., Plenum, New York (1975), p. 905.

92. M. Gettings, O. Meyer and G. Linker, Rad. Effects 21, 51 (1974).

93. Y. Quéré, Rad. Effects 28, 253 (1976).

94. D.V. Morgan and D. Van Vliet, Rad. Effects 12, 203 (1972).

95. J.U. Anderson, O. Andreasen, J.A. Davies and E. Uggerhøj, Rad. Effects 7, 25 (1971).

96. H.J. Pabst and D.W. Palmer, Proc. 5th Int. Conf. on Atomic Collisions in Solids, Plenum Press, New York, (1975) p. 141.

97. T.M. Buck and G.H. Wheatly, Surface Science, 33, 35 (1972).

98. W.H. Kool, E.H. Roosendaal, L.W. Wiggers and F.W. Saris, Rad. Effects. 36, 41 (1978).

99. J. Haskell, E. Rimini and J.W. Mayer, J. Appl. Phys. 43, 3425 (1972).

100. F.H. Eisen, J. Haskell, E. Rimini and J.W. Mayer, Proc. 3rd Int. Conf. on Ion Implantation in Semiconductors and Other Materials, Plenum Press, New York (1973), p. 99.

101. W.H. Kool, H.E. Roosendaal, L.W. Wiggers and F.W. Saris, Nucl. Instr. and Methods, 132, 285 (1976).

102. M.L.Swanson, J.A. Davies, A.F. Quenneville, F.W. Saris and L.W. Wiggers, Rad. Effects, 35, 51 (1978).

103. L.W. Wiggers and F.W. Saris, Rad. Effects, 41, 149 (1979).

104. G. Carter, private communication.

105. M.T. Robinson, The Energy Dependence of Neutron Radiation Damage in Solids, Proc. Brit. Nucl. Energy Soc. Conf. Nucl. Fusion Reactors, Abingdon, U.K. (1969), p. 364.

106. A. Amith, Phys. Rev. 116, 793 (1959).

107. C.M. Hurd, Proc. Phys. Soc. 79, 42 (1962).

108. Viktor Sergeevich Vavilov, Effects of Radiation on Semiconductors, Consultant Bureau, New York (1965).

109. J.H. Hammersley and D.C. Handscomb, Monte Carlo Methods, Methuen, London (1964).

110. R.S. Walker, Ph.D. Thesis, McMaster Univ. (1977).

111. J.A. Davies, J. Denhartog, L. Eriksson, and J.W. Mayer, CAn. J. Phys., 45, 4053 (1967).

112. J.W. Mayer, L. Eriksson, S.T. Picraux,and J.A. Davies, Can. J. Phys. 46, 663 (1968).

113. J.K. Hirvonen, W.L. Brown and P.M. Goltin, Proc. II Int. Conf. on Ion Implantation, (eds. Ruge and Graul), Springer-Verlag, p. 8 (1971).

114. F.H. Eisen and B. Welch, Proc. European Conf. on Ion Implantation, Peter Peregrinus, p. 227, (1970).

115. F.L. Vook, Radiation Damage and Defects in Semiconductors, (ed. J.E. Whitehouse), Inst. Phys. Conf., Series No. 16, p. 60 (1973).

116. H. Muller, K. Schmid, H. Ryssel and I. Ruge, Ion Implantation in Semiconductors and Other Materials. (ed. B.L. Crowder), Plenum Press, N.Y. (1973).

117. M.L. Swanson, J.R. Parsons, and J.W. Hoelke, Radiation Effects in Semiconductors (eds. Corbett and Watkins), Gordon and Breach, N.Y. p. 359 (1971).

118. J.F. Gibbons, Proc. IEEE, 60, 1062 (1972).

119. F.L. Book and H. J. Stein, Proc. First In t. Conf. on Ion Implantation (eds. Chadderton and Eisen), Gordon and Breach, N.Y.,p. 10 (1971).

120. D.A. Thompson, A. Golanski, K.H. Haugen, D.V. Stevanovic, G. Carter and C.E. Christodoulides, Rad. Eff., 52, 69 (1980).

121. D.J. Mazey, R.S. Nelson and R.S. Barnes, Phil. Mag., 17, 1145 (1968).

122. C.E. Baranova, M. M. Gusev, Yu. V. Martyneko, C.V. Starinin, and I.B. Khaibullin, Rad. Eff.,18, 21 (1973).

123. N.A. Sobolev, G. Gotz, W. Karthe and Schnabel, Rad. Eff., 42, 38 (1979).

124. D.A. Thompson, R.S. Walker and J.A. Davies, Rad. Eff., 32, 135 (1977).

125. D.A. Thompson and R.S. Walker, Rad. Eff., 36, 91 (1978).

126. J.A. Moore, G. Carter and A.W. Tinsley, Rad. Eff., 25, 49 (1975).

126. D.V. Stevanovic, private communication.

127. C.E. Christodoulides, N.J. Kadhim and G. Carter, Rad. Eff., 52, 225 (1980).

128. G. Carter and R. Webb, Rad. Eff. Lett., 43, 1 (1979).

129. S.T. Picraux, Defects in Semiconductors, eds. Narayan and Tan, p. 135 (1981).